

FORMATION OF THE ACTIVE STAR FORMING REGION LHA 120-N 44 TRIGGERED BY TIDALLY-DRIVEN COLLIDING HI FLOWS

KISETSU TSUGE,¹ HIDETOSHI SANO,^{1,2} KENGO TACHIHARA,¹ CAMERON YOZIN,³ KENJI BEKKI,³ TSUYOSHI INOUE,¹
NORIKAZU MIZUNO,⁴ AKIKO KAWAMURA,⁴ TOSHIKAZU ONISHI,⁵ AND YASUO FUKUI^{1,2}

¹*Department of Physics, Nagoya University, Furo-cho, Chikusa-ku, Nagoya 464-8601, Japan; tsuge@a.phys.nagoya-u.ac.jp*

²*Institute for Advanced Research, Nagoya University, Furo-cho, Chikusa-ku, Nagoya 464-8601, Japan*

³*ICRAR, M468, The University of Western Australia, 35 Stirling Highway, Crawley Western Australia 6009, Australia*

⁴*National Astronomical Observatory of Japan, Mitaka, Tokyo 181-8588, Japan*

⁵*Department of Physical Science, Graduate School of Science, Osaka Prefecture University, 1-1 Gakuen-cho, Naka-ku, Sakai, Osaka 599-8531, Japan*

(Accepted November 30, 2018)

ABSTRACT

N44 is the second active site of high mass star formation next to R136 in the Large Magellanic Cloud (LMC). We carried out a detailed analysis of HI at 60 arcsec resolution by using the ATCA & Parkes data. We presented decomposition of the HI emission into two velocity components (the L- and D-components) with the velocity separation of $\sim 60 \text{ km s}^{-1}$. In addition, we newly defined the I-component whose velocity is intermediate between the L- and D-components. The D-component was used to derive the rotation curve of the LMC disk, which is consistent with the stellar rotation curve (Alves & Nelson 2000). Toward the active cluster forming region of LHA 120-N 44, the three velocity components of HI gas show signatures of dynamical interaction including bridges and complementary spatial distributions. We hypothesize that the L- and D-components have been colliding with each other since 5 Myrs ago and the interaction triggered formation of the O and early B stars ionizing N44. In the hypothesis the I-component is interpreted as decelerated gas in terms of momentum exchange in the collisional interaction of the L- and D-components. In the N44 region the *Planck* sub-mm dust optical depth is correlated with the HI intensity, which is well approximated by a linear regression. We found that the N44 region shows a significantly steeper regression line than in the Bar region, indicating less dust abundance in the N44 region, which is ascribed to the tidal interaction between the LMC with the SMC 0.2 Gyrs ago.

Keywords: galaxies: Magellanic Clouds — galaxies: ISM — galaxies: star formation — ISM: atoms
— ISM: HII regions — stars: massive

1. INTRODUCTION

1.1. High-mass star formation

The formation mechanism of high-mass stars is one of the most important issues in astronomy, because their extremely energetic interactions with surrounding material, in the form of UV radiation, stellar winds, and supernova explosions, are influential in driving galaxy evolution. Two models, the competitive accretion and the monolithic collapse have been major theoretical schemes of high-mass star formation (see for reviews, Zinnecker & Yorke 2007; Tan et al. 2014). In spite of the numerous studies, we have not understood detailed mechanisms of high-mass star formation.

Recently, the cloud-cloud collision model (the CCC model; Habe & Ohta 1992; Anathpindika 2010) attracted attention as a mechanism of high-mass star formation and observational studies showed that more than 30 regions of high-mass stars and/or clusters are triggered by cloud-cloud collision: NGC 1333 (Loren 1976), Sgr B2 (Hasegawa et al. 1994; Sato et al. 2000), West-erlund 2 (Furukawa et al. 2009; Ohama et al. 2010), NGC 3603 (Fukui et al. 2014c), RCW 38 (Fukui et al. 2016), M 42 (Fukui et al. 2018a), NGC 6334/NGC 6357 (Fukui et al. 2018b), M17 (Nishimura et al. 2018), W49 A (Miyawaki et al. 1986, 2009), W51 (Okumura et al. 2001; Fujita et al. 2017), W33 (Kohno et al. 2018a), M20 (Torii et al. 2011, 2017a), RCW 120 (Torii et al. 2015), [CPA2006] N37 (Baug et al. 2016), GM 24 (Fukui et al. 2018d), M16 (Nishimura et al. 2017), RCW 34 (Hayashi et al. 2018), RCW 36 (Sano et al. 2018), RCW 32 (Enokiya et al. 2018), RCW 166 (Ohama et al. 2018a), Sh2-48 (Torii et al. 2017c), Sh2-252 (Shimoikura et al. 2013), Sh2-235, 237, 53 (Dewangan et al. 2016, 2017a, 2018a), LDN 1004E in the Cygnus OB 7 (Dobashi et al. 2014), [CPA2006] S 36 (Torii et al. 2017b), [CPA2006] N35 (Torii et al. 2018), [CPA2006] N4 (Fujita et al. 2018), [CPA2006] S44 (Kohno et al. 2018b), [CPA2006] N36 (Dewangan et al. 2018b), [CPA2006] N49 (Dewangan et al. 2017b), LHA 120-N159 West (Fukui et al. 2015), [CPA2006] S 116 (Fukui et al. 2018c), LDN 1188 (Gong et al. 2017), LDN 1641-N (Nakamura et al. 2012), Serpens South (Nakamura et al. 2014), NGC 2024 (Ohama et al. 2017a), RCW 79 (Ohama et al. 2018b), LHA 120-N159 East (Saigo et al. 2017), NGC 2359 (Sano et al. 2017), Circinus-E cloud (Shimoikura & Dobashi 2011), G337.916 (Torii et al. 2017b), Rosette Molecular Cloud (Li et al. 2018), Galactic center (Tsuboi et al. 2015), G35.2N & G35.2S (Dewangan 2017), NGC 2068/NGC 2071 (Tsutsumi et al. 2017), NGC 604 (Tachihara et al. 2018) These studies lend support for the role of cloud-

cloud collision which triggers formation of O stars. A typical collision size scale and relative velocity between the two clouds are 1–10 pc and 10–20 km s⁻¹ and the number of O-type stars formed by the collision is in a range from 1 to ~20 for H₂ column density greater than 10²² cm⁻². The CCC model realizes gas compression by two orders of magnitude within 10⁵ yrs (~1 pc/10 km s⁻¹) and provides a high mass accretion rate by supersonic collision between molecular clouds. These phenomena clearly creates physical conditions which favor high-mass star formation according to theoretical simulations of the collisional process in the realistic inhomogeneous molecular gas (Inoue & Fukui 2013; Inoue et al. 2018), whereas it remains to be observationally established how unique and common the role of the collisions is in the O-type star formation. In this context we note that a large-scale model of molecular cloud evolution via collision demonstrates the important role of collision in star formation and cloud growth (Kobayashi et al. 2018).

One of the observational signatures of cloud-cloud collisions is complementary distribution between the two colliding clouds. It is usual that the colliding two clouds have different sizes as simulated by theoretical studies (Habe & Ohta 1992; Anathpindika 2010; Takahira et al. 2014). If one of the colliding clouds is smaller than the other, the small cloud creates a cavity of its size in the large cloud through the collision. The cavity is observed as an intensity depression in the gas distribution at a velocity range of the large cloud, and the distributions of the small cloud and the cavity exhibit a complementary spatial distribution. The complementary distributions often have some displacement because the relative motion of the collision generally makes a non-negligible angle to the line of sight. Fukui et al. (2018a) presented synthetic observations by using the hydrodynamical numerical simulations of Takahira et al. (2014). In the previous works, there are more than 6 regions where the displacement was well determined, including M17 (Nishimura et al. 2018), M42 (Fukui et al. 2018a), RCW 36 (Sano et al. 2018), GM 24 (Fukui et al. 2018d), S 116 (Fukui et al. 2018c), R136 (Pape I).

The collisional process on a few–10 pc scale were investigated by Magnetohydrodynamic (MHD) numerical simulations. These simulations show that the H I gas flow colliding at 20 km s⁻¹ is able to compress H I gas and the density of H I gas is enhanced in the compressed layer (Inoue & Inutsuka 2012). Molecular clouds are formed in the shock-compressed layer in a time scale of ~10 Myr, which can probably become shorter to a few Myr when the colliding velocity is as fast as 100 km s⁻¹ if density is higher. These clouds will become self-gravitating

when they grow massive enough. Inoue & Fukui (2013) and Inoue et al. (2018) calculated the subsequent physical process where two molecular gas flows collide at 20 km s^{-1} . These studies show that strong shock waves generated by a cloud-cloud collision form gravitationally unstable massive molecular cores, each of which directly leads to form a high-mass star.

1.2. Previous study of the LMC

In the context of cloud-cloud collision, the nearest galaxies to the Galaxy, the LMC and the SMC, provide an excellent laboratory to test star formation and the collisional triggering. Luks & Rohlfs (1992) separated two HI velocity components of the LMC whose velocity difference is $\sim 50 \text{ km s}^{-1}$; one is the HI gas extending over the whole disk of the LMC (hereafter D-component) and the other more spatially confined HI having lower radial velocity (hereafter L-component). They analyzed the HI data obtained by Parkes telescope with angular resolution and grid size of $15'$ and $12'$, respectively, and they found that the D- and L-components contain 72 % and 19 % of the whole HI gas, respectively. In spite of the work by Luks & Rohlfs (1992), the implications of the two components on star formation was not observationally explored for nearly two decades.

Recently it was found that the young massive cluster RMC136 (R136) in the Large Magellanic Cloud (LMC) is located toward an overlapping area of the L- and D-components (Fukui et al. 2017, ;hereafter Paper I). These authors analyzed the HI data of the whole LMC at a $1'$ resolution which corresponds to 15 pc at a distance of the LMC (Kim et al. 2003), and separated the L- and D-components at a higher resolution. Figure 1 shows a typical HI spectrum which presents the L- and D-components. The authors of paper I revealed that the two components are linked by the bridge features in the velocity space and show complementary spatial distributions on a kpc scale. Based on these two signatures it was suggested that the L- and D-components are colliding toward R136, and a scenario was presented that the collision of the HI flows triggered the formation of the R136 cluster and high mass stars in its surroundings. They also showed that a component having intermediate velocity between the L- and D-components (hereafter I-component), and indicated that the I-component may represent merging of the L- and D-components where their relative velocity is decelerated with momentum conservation (see Figure 2 of Paper I). According to the theoretical studies including hydrodynamical numerical simulations, the LMC and SMC had a close encounter 0.2 Gyr ago and their tidal interaction stripped gas from the two galaxies. Currently the remnant gas is

falling down to each galaxy, and observed as the HI gas with significant relative velocity (Fujimoto & Noguchi 1990; Bekki & Chiba 2007a; Yozin & Bekki 2014).

1.3. LHA 120-N 44

We extend the study from R136 to other active HII regions in the LMC and to test how the colliding gas flow leads to massive star formation. Following Paper I, we analyze the region of LHA 120-N 44 (N44) in the present paper. N44 is the HII region cataloged by Henize (1956) and is one of the most active star-forming regions in the LMC. N44 is older (5–6 Myr: Will et al. 1997) than R136 (1.5–4.7 Myr: Schneider et al. 2018). N44 holds the second largest number of O / WR stars, ~ 40 , corresponding to $\sim 1/10$ of R136 (Bonanos et al. 2009), in the LMC, and N44 has received much attention at various wavelengths from mm/sub-mm, infrared, optical to high-energy X-rays (e.g., Kim et al. 1998c; Chen et al. 2009; Carlson et al. 2012). This region is also categorized as a superbubble by a H α shell, and the OB association LH 47 is located in the center of the shell. Ambrocio-Cruz et al. (2016) investigated kinematic features of H α emission and compared it with the L- and D-components. These authors showed that compact HII regions N44B and C have two H α components with a velocity difference of $\sim 30 \text{ km s}^{-1}$, and interpreted that N44B and C belong to the L- and D-components, respectively. Kim et al. (1998c) analyzed the high-resolution HI data toward N44 and indicated that the HI shell corresponding to the H α shell was produced by stellar winds and supernovae, whereas the relationship between the shells and the L- and D-components remain unknown. These previous studies show that the N44 region is the most suitable target for studying high mass star formation next to R136.

The present paper is organized as follows; Section 2 summarizes the data sets and methodology and Section 3 the results. The discussion is given in Section 4, in which we test whether the high-mass star formation in N44 have been triggered by the colliding HI flows. Section 5 gives a summary.

2. DATA SET AND MASKING

2.1. Data sets

2.1.1. HI

Archival data of the Australia Telescope Compact Array (ATCA) and Parkes HI 21 cm line emission are used (Kim et al. 2003). The angular resolution of the combined HI data is $60''$ ($\sim 15 \text{ pc}$ at the LMC). The rms noise level of the data is $\sim 2.4 \text{ K}$ for a velocity resolution of 1.649 km s^{-1} . They combined the HI data obtained by ATCA (Kim et al. 1998a) with the these obtained with

the Parkes multibeam receiver with resolution of $14' - 16'$ (Staveley-Smith 1997). This is because the ATCA is not sensitive to structures extending over $10' - 20'$ (150–160 pc) due to the minimum baseline of 30 m.

2.1.2. *Planck/IRAS*

Archival datasets of the dust optical depth at 353 GHz (τ_{353}) and dust temperature (T_d) were obtained by using the combined *Planck/IRAS* data with the gray-body fitting. For details, see Planck Collaboration et al. (2014). These datasets are used to make comparison with the HI data. The angular resolution is $5'.0$ (~ 75 pc at the LMC) with a grid spacing of $2'.4$. For comparison of τ_{353} with HI, the spatial resolution and the grid size of HI were adjusted to τ_{353} .

2.1.3. CO

We used $^{12}\text{CO}(J=1-0)$ data of the Magellanic Mopra Assessment (MAGMA; Wong et al. 2011) for a small-scale analysis in the N44 region. The effective spatial resolution is $45''$ (11 pc at a distance of 50 kpc), and the velocity resolution is 0.526 km s^{-1} . The MAGMA survey does not cover the whole LMC and the observed area is limited toward the individual CO clouds detected by NANTEN (Fukui et al. 1999; Mizuno et al. 2001).

We used the data of the $^{12}\text{CO}(J=1-0)$ observed over the whole LMC with the NANTEN 4-m telescope at a resolution of $2'.6$, a grid spacing of $2'.0$, and velocity resolution of 0.65 km s^{-1} (Fukui et al. 1999, 2008; Kawamura et al. 2009). In the present paper, the NANTEN data were used to mask the CO emitting regions in comparing the *Planck/IRAS* data with the HI.

2.1.4. $H\alpha$

$H\alpha$ data of the Magellanic Cloud Emission-Line Survey (MCEL; Smith & MCELS Team 1999) are used for a comparison of spatial distribution with HI. The dataset was obtained with a 2048×2048 CCD camera on the Curtis Schmidt Telescope at Cerro Tololo Inter-American Observatory. The angular resolution is $\sim 3'' - 4''$ ($\sim 0.75 - 1.0$ pc at distance of 50 kpc). We also use the archival data of $H\alpha$ provided by the Southern H-Alpha Sky Survey Atlas (SHASSA; Gaustad et al. 2001) in order to define the region where UV radiation is locally enhanced. The same method was also applied in Paper I, and hence we can compare the result of R136 with that of N44. The angular resolution is about $0'.8$, and the sensitivity level is 2 Rayleigh ($1.2 \times 10^{-17} \text{ erg cm}^{-2} \text{ s}^{-1} \text{ arcsec}^{-2}$) pixel^{-1} .

2.2. Masking

We masked some regions in the distribution of the dust optical depth at 353 GHz (τ_{353}) in order to avoid

the effect of local dust destruction by the ultraviolet (UV) radiation from O-type stars/HII regions in comparison of τ_{353} with HI. Such a local effect may alter the dust properties which is assumed to be uniform in the comparison, and can distort the correlation between HI and dust emission. By using CO and $H\alpha$ data, the regions with CO emission higher than 1 K km s^{-1} ($\sim 1\sigma$) with $H\alpha$ emission higher than 30 Rayleigh are masked as made in the previous works (Fukui et al. 2014b, 2015; Okamoto et al. 2017).

3. RESULTS

3.1. Method of HI spectral decomposition

In Paper I HI gas decomposition into the L- and D-components were demonstrated, but details were not given. We here describe a detailed method of the decomposition used in the present paper and in Paper I in the Appendix. In order to decompose the HI spectra into the L- and D-components, we made Gaussian fittings to the HI data. We fitted the Gaussian function to the HI emission lines for each pixel with peak intensity greater than 20 K and derived the peak velocity of the spectrum. This process allowed us to derive the velocity of the D-component toward the areas where the L-component is weaker than the D-component. For the profiles showing the L-component as the primary peak we made another fitting to the secondary peak and define the D-component if the secondary peak velocity is larger than the primary peak. We thus obtained distribution of the D-component over the disk. The result was used to derive the rotation velocity of the disk. Then, we subtracted the rotation velocity for each pixel by shifting the spectra in the velocity channel over the LMC. We defined the V_{offset} as the relative velocity to the D-component as follows: $V_{\text{offset}} = V_{\text{LSR}} - V_D$ (V_D = the radial velocity of the D-component). Hereafter, we use V_{offset} instead of V_{LSR} in the following.

We determined the typical velocity ranges of the L- and D-components as V_{offset} from -100 to -30 km s^{-1} and from -10 to $+10 \text{ km s}^{-1}$, respectively, over the whole galaxy from position-velocity diagrams, and velocity channel map in Paper I. We also defined the intermediate velocity between the L- and D-components in a range of V_{offset} from -30 to -10 km s^{-1} (I-component). The maximum variation of velocity range is about $\pm 10 \text{ km s}^{-1}$.

We note that these velocity ranges vary from region to region, which require fine tuning in the individual regions due to velocity variation of the L-component.

3.2. The rotation curve of the LMC

We derived the rotation curve of the LMC represented by the velocity distribution of the D-component as shown in Figure 2c. As described in the Appendix B, we optimized the coordinate of rotation center, the inclination angle of the galaxy disk plane, and the position angle of the inclination axis. The present curve shows the flat rotation of the LMC with the constant rotation velocity of $\sim 60 \text{ km s}^{-1}$ at the galactocentric radius (R_G) is larger than 1 kpc, and is consistent with the stellar disk rotation as shown in Figure 2c. The previous rotation velocity of HI (Kim et al. 1998a) decreases at $R_G > 2.5 \text{ kpc}$. Kim et al. (1998a) did not consider the two velocity components and their rotation velocity is from a mixture of the L- and D-components. Moreover, it is likely that the extended emission was resolved out since they used the HI data taken with the ATCA alone. In the present study, we used the combined with ATCA and Parkes HI data and the missing flux is recovered.

3.3. Distribution of the L- and D-components

We compare HI distribution with the major star forming regions over the whole LMC. Figures 3a and 3b present distributions of the L- and D-components, and Figure 3c an overlay of the two components. The L-component distribution is concentrated in two regions. One of them is the HI Ridge stretching by $\sim 1 \text{ kpc} \times 2.5 \text{ kpc}$ in R.A. and Dec., including young star forming regions R136 and LHA 120-N 159. The other region is extended to the northwest from the center of the LMC with a size of $\sim 2 \text{ kpc} \times 2 \text{ kpc}$ including LHA 120-N 44 (hereafter diffuse L-component). The mean intensity of the diffuse L-component is $\sim 40 \%$ of that of the HI Ridge. Several HII regions (Ambrocio-Cruz et al. 2016) are located in the south of the diffuse L-component. The D-component is extended over the entire LMC and is characterized by the morphological properties with many cavities and voids (e.g., Kim et al. 1998b; Dawson et al. 2013).

3.4. Velocity distribution of the HI gas toward the N44 region

Figure 4a shows HI total intensity distribution toward the presently analyzed region of N44. HI gas is concentrated in the region within $\sim 200 \text{ pc}$ of N44C and its HI integrated intensity is enhanced to 2000 K km s^{-1} . Figure 4b is a H α image (MCEL; Smith & MCELS Team 1999) of the star forming region indicated by a black box in Figure 4a. N44 B and N44 C are located in a shell (white dashed circle) whose central coordinate is (R.A., Dec.) $\sim (5^h 22^m 15^s, -67^\circ 57' 00'')$. The shell includes a WR-star and 35 O-type stars. In the southeast, there is another HII region N44D containing two O-type stars (Bonanos et al. 2009).

Figure 5 shows typical spectra of HI in the northeast and south of N44. There are two velocity components with V_{offset} of $\sim -60 \text{ km s}^{-1}$ and $\sim -30 \text{ km s}^{-1}$, besides the D-component. In Figure 5a, we find the L-component is peaked at -60 km s^{-1} , 10 km s^{-1} lower than that shown in Figure 1, while the D-component is peaked at 0 km s^{-1} . The L- and the D-components are connected by a bridge feature between the two velocity components. We interpret the component at $V_{\text{offset}} = -80.6 \text{--} -50.0 \text{ km s}^{-1}$ as part of the L-component, that at $V_{\text{offset}} = -50.0 \text{--} -15.6 \text{ km s}^{-1}$ as part of the I-component. In Figure 5b, no L-component is seen and we interpret that there is only the I-component at $V_{\text{offset}} = -50.0 \text{--} -15.6 \text{ km s}^{-1}$. In comparing the HI with the O-type stars we focus on Lines A, B and C in Figure 4a where most of the massive stars in N44 are concentrated.

Figure 6 shows Dec.-velocity diagrams integrated in the R.A. direction along Lines A, B, and C which have a width of $\sim 87 \text{ pc}$ and a length of $\sim 1.1 \text{ kpc}$ in Figure 4a. Lines A, B, and C pass the eastern, central, and western regions of N44, respectively. In Line A (Figure 6a), the D-component and the L-component are located at Dec. $= -67^\circ 45' 00''$ to $-68^\circ 40' 00''$ and $-67^\circ 50' 00''$ to $-68^\circ 0' 00''$, respectively. The bridge feature connects them at the position shown by a white dashed box in velocity space. In Line B (Figure 6b), the D-, and I -components are seen at Dec. $= -67^\circ 30' 00''$ to $-68^\circ 09' 00''$ and Dec. $= -68^\circ 03' 00''$ to $-68^\circ 15' 00''$, respectively. A bridge feature which is shown by a white dashed box connects them. The D-, I -, and L-components are distributed in Line C (Figure 6c). We also see bridge features like in the other Lines as indicated by white dashed boxes. At the position of Dec. $= -68^\circ 06' 00''$ to $-68^\circ 15' 00''$, the L- and D-components are connected by another bridge feature, and at Dec. $= -68^\circ 30' 00''$ - $-68^\circ 40' 00''$, the I - and D-components are connected by a bridge feature.

3.5. The spatial distribution of HI gas toward the N44 region

Detailed spatial distributions of the L-, I-, and D-components around N44 are shown in Figure 7. The L-component is distributed in the northeastern and southwestern regions of N44 (Figure 7a). The I -component is extended by $\sim 200 \text{ pc} \times 400 \text{ pc}$ in the south of N44 (Figure 7b). The D-component mainly spreads from the central region to southeast of N44 (Figure 7c).

Comparisons of spatial distributions of different velocity components are shown in Figure 8, which shows the distribution of the D-component ($-15.6 \text{--} +9.7 \text{ km s}^{-1}$) overlaid on the L-component contours. The L-component has complementary distributions with

the D-component at the positions of (R.A., Dec.) = ($5^h22^m30^s$ – $5^h24^m0^s$, $-67^d50^m0^s$ – $68^d0^m0^s$) and ($5^h20^m0^s$ – $5^h22^m30^s$, $-68^d20^m0^s$ – $68^d0^m0^s$) as indicated by black arrows. Two of the L-component exist along the edge of the D-component. We interpret that the two depressions in the D-component, which corresponds the L-components, may represent interaction between the two components. There are more intensity depressions where no corresponding L-components are seen. They are possibly due to preexistent intensity variations or created by other mechanisms like supernovae.

In Figure 9, the D-component shows intensity depression toward the I-component at the positions of (R.A., Dec.) \sim ($-67^d58^m0^s$ – $68^d36^m00^s$, $5^h18^m0^s$ – $5^h26^m00^s$) as indicated by the red box. We find some displacement of the complementary distribution between the I- and D-components, which is a usual signature caused by a certain angle of cloud-cloud collision to the line of sight (Fukui et al. 2018a). We calculated the displacement by using overlapping function $H(\Delta)$ in pc^2 which shows a degree of complementarity (Fukui et al. 2018a). We derived the projected displacement where the overlapping area of the strong I-component (intensity larger than 550 K km s^{-1}) and the depression of the D-component (intensity smaller than 1100 K km s^{-1}) becomes maximum.

In Figure 9b the I-component is surrounded by the D-component at (R.A., Dec.) = ($-68^d4^m0^s$ – $68^d42^m00^s$, $5^h18^m0^s$ – $5^h26^m00^s$) as indicated by the black box. They present complementary distribution with a displacement of 107 pc and a position angle of 180 deg.

Figure 10 shows an enlarged view of the N44 region, showing complementary distributions among the D-, I-, and L-components at a ~ 100 pc scale. The D- and I-components have complementary distribution at (R.A., Dec.) \sim ($5^h21^m30^s$ – $5^h24^m0^s$, $-68^d5^m0^s$ – $68^d10^m0^s$) and the L- and D-components show complementary distribution at (R.A., Dec.) \sim ($5^h23^m0^s$ – $5^h23^m36^s$, $-67^d58^m0^s$ – $67^d52^m0^s$) and ($5^h20^m30^s$ – $5^h21^m30^s$, $-68^d10^m0^s$ – $68^d5^m0^s$). At (R.A., Dec.) \sim ($5^h22^m30^s$, $-67^d56^m00^s$), an HI cavity of a ~ 20 pc radius is seen. It is suggested that the HI cavity indicates dynamical effects of stellar winds and supernova explosions (Kim et al. 1998c). There is only the D-component within ~ 60 pc of the HI cavity.

3.6. Physical properties and the distribution of massive stars

We calculate the mass and column density on an assumption that HI emission is optically thin. We use the equation as follows (Dickey & Lockman 1990):

$$N_{\text{HI}} = 1.8224 \times 10^{18} \int \Delta T_b dv [\text{cm}^{-2}], \quad (1)$$

where T_b is the observed HI brightness temperature [K].

The physical properties of HI gas along Lines A, B, and C (width: ~ 70 pc, length: ~ 360 pc) shown in Figure 10 are summarized in Table 1. We integrated all the velocity range ($-100.1 < V_{\text{offset}} < 89.7 \text{ km s}^{-1}$) for estimating mass and column density of HI gas. The mass and column density of Lines A, B, and C show similar values. The mass is about $10^6 M_\odot$ and the peak column density is about $6 \times 10^{21} \text{ cm}^{-2}$. The velocity separations between the two velocity components in Lines A, B, and C are about 20 to 60 km s^{-1} . The bridge features are observed in Lines A, B, and C. Most of the massive stars (WR and O-type stars) are located in Line B. Figure 11 shows a histogram of the number of massive stars around the N44 region in Figure 10. We counted the number of WR and O-type stars located inside the areas of Lines A, B, and C (e.g., Bonanos et al. 2009). Lines A, B, and C have 2, 32, and 5 massive stars, respectively.

We calculate the mass of the L-, I-, and D-components toward the N44 region in Figure 10. Table 2 summarizes the physical quantities around N44. We used equation (1) for the calculation of HI parameters in the same method as in Table 1. The total mass is $\sim 3.0 \times 10^6 M_\odot$ and the mass of the D-component occupies 2/3 of the total mass.

H_2 gas mass was estimated by using the $W_{\text{CO}}\text{--}N(\text{H}_2)$ conversion factor ($X_{\text{CO}} = 7.0 \times 10^{20} \text{ cm}^{-2} (\text{K km s}^{-1})^{-1}$; Fukui et al. 2008). We use the equation as follows:

$$N(\text{H}_2) = X_{\text{CO}} \times W(^{12}\text{CO}(J=1-0)), \quad (2)$$

where W_{CO} is the integrated intensity of the $^{12}\text{CO}(J=1-0)$ and $N(\text{H}_2)$ is the column density of molecular hydrogen. The total mass of H_2 gas is $\sim 3.0 \times 10^6 M_\odot$. Most of CO clouds are included in the D-component.

3.7. Comparison with dust emission

We compared the intensity of HI (W_{HI}) and the dust optical depth at 353 GHz (τ_{353}) in order to investigate the gas to dust ratio. Figure 12 shows a typical spectrum of HI (HI4PI Collaboration et al. 2016) toward the LMC. There is a Galactic foreground component at $-50 < V_{\text{LSR}} < +50 \text{ km s}^{-1}$, while HI emission in $+150 < V_{\text{LSR}} < +350 \text{ km s}^{-1}$ belongs to the LMC. Because τ_{353} does not have velocity information, we subtracted

the foreground dust optical depth from τ_{353} by assuming that the foreground HI emission is optically thin and its $W(\text{HI})$ is proportional to τ_{353} using $W_{\text{HI}}\text{--}\tau_{353}$ relation in the Galaxy (Fukui et al. 2015) as follows:

$$W_{\text{HI}}[\text{K km s}^{-1}] = 1.15 \times 10^8 [\text{K km s}^{-1}] \times \tau_{353} \quad (3)$$

It is also possible to subtract the Galactic foreground by using an uniform Galactic foreground contamination using the averaged τ_{353} value around the LMC. However, it is not appropriate to use the data around the LMC, because HI gas is faint but widely extend around the LMC like as the Magellanic Bridge and the Magellanic Stream (Putman et al. 1998). On the other hand, as shown in Figure 12, it is better to estimate the Galactic foreground from HI data since HI gas can be clearly separated into the foreground component and the LMC component by using velocity information. Figures 13a and 13c show the spatial distributions of τ_{353} before and after subtracting the Galactic foreground, respectively. In addition, the Galactic foreground is considerably weaker than the LMC component, so the subtraction is made fairly accurately. The Galactic foreground accounts for 30% or less of the total τ_{353} in the main regions of the LMC (Figure 13b, d).

First, we smooth the spatial resolution of HI to the same resolution as τ_{353} , $5'$, and subtract the foreground from the total τ_{353} for each pixel. We use only the LMC component for a comparison between the HI data and τ_{353} after the subtraction of the foreground component. Figure 14 shows a scatter plot between W_{HI} and τ_{353} for each pixel. The gray diamonds and the red circles indicate data points of the Bar region (Paper I) and that of the N44 region (Figure 4a), respectively. The values of τ_{353} in the LMC are small ($<10^{-4}$) and the dust emission is optically thin. Therefore, τ_{353} reflects the column density of hydrogen atoms and is proportional to W_{HI} under the assumptions of (1) HI emission is optically thin, (2) dust mixes well with gas, and (3) dust optical properties are uniform. On the other hand, saturation of W_{HI} is caused when the atomic gas becomes colder and denser. It is thought that HI is optically thin at high temperature because the absorption coefficient of the HI emission is inversely proportional to the spin temperature. We use HI data which keep a proportional relation between W_{HI} and τ_{353} . In this paper, we assumed that HI gas is optically thin for the data points of T_d is high (22–24.5 K). Dust temperature (T_d) varies from region to region. So, we used HI gas at $T_d > 22.5$ K in the Bar region, and used HI gas data for $T_d > 24.5$ K in the N44 region.

The ratio of $W(\text{HI}) / \tau_{353}$ is an indicator of the gas-dust ratio under the above assumptions of (1)–(3). We derived the slope between $W(\text{HI})$ and τ_{353} by the least-squares fit which is assumed to have a zero intercept. The black and red linear lines indicate the fitting results of the Bar region and that of the N44 region, respectively. The slope of the Bar region is 7.6×10^7 K km s $^{-1}$ and that of N44 region is 1.0×10^8 K km s $^{-1}$ showing difference of slopes by a factor of 1.3. This implies that the metallicity in the N44 region is lower than that in the Bar region, a trend similar to the HI ridge (Paper I). This result is discussed in Section 4.3. The dispersion of the Bar region looks larger than the N44 region. This means that there may be metallicity gradient in the Bar region. We will present the detailed gas to dust ratio of the whole LMC in following paper (K. Tsuge et al. in preparation).

4. DISCUSSION

4.1. Evidence for the collision of HI between the two velocity components

We revealed the spatial and velocity distributions of the L- ($V_{\text{offset}} = -80.6$ – -50.0 km s $^{-1}$), I- ($V_{\text{offset}} = -50.0$ – -15.6 km s $^{-1}$), and D- ($V_{\text{offset}} = -15.6$ – $+14.9$ km s $^{-1}$) components by using high-resolution HI data. These results show the signatures of collision toward N44 between the HI flows in a similar fashion for the HI Ridge and R136 in Paper I.

In Paper I, it was shown that the complementary spatial distribution between the L- ($V_{\text{offset}} = -100.1$ – -30.5 km s $^{-1}$) and the D-components ($V_{\text{offset}} = -10.4$ – $+9.7$ km s $^{-1}$) at a kpc scale. It was also noted that the L- and D-components are connected by the bridge features in velocity space. These results give evidence of collision between the L- and D-components, suggesting that the collision of the HI gas triggered the formation of ~ 400 O /WR stars in the HI Ridge which includes R136, N159, and the other active star forming giant molecular clouds (Paper I). The observational signatures of high-mass star formation by colliding HI flows are characterized by the three elements: (1) the two velocity components with a supersonic velocity separation, (2) the bridge features which connect the two velocity components in velocity space, and (3) the complementary spatial distribution between the two HI flows. In order to test whether the high-mass star formation in N44 have been triggered by the colliding HI flows, we compared the above signatures with the observational results for N44.

4.1.1. The supersonic velocity separation

In N44, the velocity separation of the two components is about 30 to 60 km s⁻¹ (Figure 5). If we consider a projection effect, the actual velocity separation is larger than observed. These large velocity separations cannot be explained by the stellar winds and UV radiation from the high-mass stars, where the typical stellar feedback energy is less than 10% of the kinematic energy of the colliding flows (Paper I). As we mentioned in section 1.3, Kim et al. (1998c) found that there are two clear intensity depressions of H I gas and expanding shells of H I gas by small-scale (hundreds pc) analysis (shown in Figures 2 and 4 of their paper). However, we did not find obvious expansion structures in a kpc scale analysis (Figure 6). Figure 15 shows the second moment map of the D-component ($-15.6 < V_{\text{offset}} < +14.9$ km s⁻¹). The average velocity dispersion is ~ 7.6 km s⁻¹ and there is no spatial correlation between the H α shell (dashed circle) and velocity dispersion (Figure 15a). Moreover, it is impossible to explain the motion of the L-, I-, and D-components by expanding shell from the compact area of energy supply. We calculated the kinematic energy of the H I gas as $\sim 10^{53}$ erg by assuming the expansion velocity is 30 km s⁻¹. So, the kinematic energy of a super bubble is insufficient to explain the velocity distribution of the H I gas. Moreover, it requires ~ 2000 supernova explosions (SNe) within the age of N44 if we assume that kinematic energy injection by SNe is transferred in gas acceleration by $\sim 5\%$ (Kruijssen 2012). This number of SNe is much larger than ~ 300 which is expected from the scale of the super bubble N44 (Meaburn & Laspias 1991).

On the other hand, it is seen that the velocity dispersion of the D-component increases toward the region where the I-component is located as shown in Figure 15b. This suggests that the collision between H I flows played a role in creating the observed gas motion.

4.1.2. The bridge features in velocity space

As seen in Figure 6, there are I-component between the two velocity components. These signatures indicate that the two velocity components interact dynamically with each other in spite of the large velocity separation, which otherwise may suggest a large spatial separation and no interaction between the two in space.

4.1.3. Complementary spatial distribution

We revealed the detailed spatial distributions of the L-, I-, and D-components, and compared their spatial distributions. In Figure 9 the complementary spatial distribution is found not only between the L- and D-components (Figure 8) but also between the I- and D-components, whereas the I-component partly overlaps

the D-component (Figure 9a). In Figure 8, the L- and D-components show complementary spatial distribution. The L-component is distributed clearly along the edge of the D-component in the northeast and southwest of N44. The I- and D-components show some complementary spatial distribution, while the I-component partly overlaps with the D-component in the south of N44 D as shown in Figure 9b.

A possible interpretation of these spatial distributions is deceleration of the H I gas by momentum conservation in the interaction. In the R136 region, we interpreted that the L-component penetrated into the D-component with small deceleration when the D-component has lower column density than the L-component, whereas the L- and D-components merge together with significant deceleration where they have nearly the same column density. The difference in the column density of colliding H I flows then affects the velocity in the merged components by momentum conservation (Paper I). If we assume a similar collisional process, the distributions of H I gas can be interpreted as follows; In the northeast and southwest of N44, two parts of the L-component are located where the intensity of the D-component is weaker than the surroundings (Figure 8). The average column density of the D-component in this region is $\sim 1.7 \times 10^{21}$ cm⁻². It is likely that the L-component exhibits weakly a sign of deceleration, because $N(\text{H I})$ of the L-component dominates that of the D-component when momentum conservation is considered. The initial column density of the L-component was probably high enough toward the region. In the south of N44, the I-component overlaps with the D-component which has the highest intensity of H I (Figure 9a). The maximum column density of the D-component is $\sim 4.0 \times 10^{21}$ cm⁻². We suggest that $N(\text{H I})$ of the L- and D-components was nearly the same, and that the collision resulted in merging of the two components at an intermediate velocity of these components. The total $N(\text{H I})$ of the merged component was then elevated to $\sim 6 \times 10^{21}$ cm⁻² due to the merging. In the other regions, the I- and D-components show complementary spatial distribution, a characteristic of collision between the two components. The I-component exists but is weak in H I in the north of N44B and C as shown in Figure 9a. This is probably because the stellar ionization already dispersed the colliding H I gas. The age of N44 (5–6 Myr; Will et al. 1997) is three times older than that of R136. We suggest the two components are colliding as well as in the other areas of N44.

Another possible interpretation is displacement of the colliding two velocity components. It is usually the case that the angle of the colliding two clouds is not 0° rel-

ative to the line of sight. This collision angle θ makes a displacement of the complementary distribution between intensity depression of the D-component and the dense part of the I-component according to the time elapsed since the initiation of the collision. Thus, we are able to see the overlap of the I- and D-components in the south of N44 D shown in Figure 9a, and the overlap is considered to be due to the projection. In Figure 9b where is applied a displacement of 107 pc as shown by an arrow in Figure 9. We see the I-component better fits the edge of the D-component than in Figure 9a and they exhibit complementary distribution. In order to estimate the optimum displacement, we applied the method which is presented in Fukui et al. (2018a). We calculated the overlap integral $H(\Delta)$ in pc^2 , which is a measure of the overlapping area of the strong I-component (Integrated intensity $> 550 \text{ K km s}^{-1}$) and the depression of the D-component (Integrated intensity $< 1100 \text{ K km s}^{-1}$).

We then searched for the best optimal solution of displacement to maximize the overlapping integral $H(\Delta)$ sweeping the I-component in position as a cross correlation function. The sweeping was done toward 5 different directions of Δ -axis with the position angle from 170° to 190° with 5° steps, and by the Δ offsets from -400 to $+400 \text{ pc}$ with 9.7 pc steps. It was then found that the Δ -axis of 180° and $\Delta=107 \text{ pc}$ gives the largest $H(\Delta)$ value as shown in Figure 9c. This displacement is indicated in Figure 9b by the arrow, and by the good complementary distributions between the strong I-component and the depressed D-component. More details about $H(\Delta)$ are given in Appendix of Fukui et al. (2018a).

The I-component partly overlaps with the D-component, for example at (R.A., Dec.) $\sim (5^h25^m0^s, -68^d20^m0^s)$ after applying the displacement. We note that the complementary distribution may not hold so strictly, depending on the three-dimensional spatial distributions of the D-component, and that the I-component may overlap in part the D-component, depending on the initial distribution of the two components.

These characteristics (Sections 4.1.1–4.1.3) are consistent with the observational signatures of collision between the HI flows shown in Paper I and lend support that the colliding HI flows triggered the formation of ~ 40 high-mass stars in N44 as in the R136 region.

4.2. Stellar properties and crossing timescale

In the previous section, we presented a scenario for massive star formation by colliding HI flows in N44. In this sub-section, we discuss the stellar properties, the star formation rate, and the crossing timescale in the context of the scenario. Crossing timescale is the time

it takes for the L- or I-components to pass through the D-component in collision.

4.2.1. Distribution of high-mass stars and physical properties of HI gas

In Figure 10, we see that most of the high-mass stars are formed in the central region of N44 where HI flow is colliding (Line B in Figure 10). We suggest that the high-mass stars were mostly formed by colliding HI flows in Line B, if HI flows are decelerated by the collision and become further compressed. In the Dec.-Velocity diagrams of the central region of N44 (Figure 6), the velocity separation between the two components in Line B is smaller than in Lines A and C where the velocity separation is $\sim 50 \text{ km s}^{-1}$, while in Line B the velocity separation is $\sim 20 \text{ km s}^{-1}$. This difference in the velocity separation suggests that the L-component is significantly decelerated by the collision between the D-component in Line B, leading to the most significant HI gas compression.

We calculated the total HI mass and peak column density in Lines A, B, and C in Figure 10 and did not find significant difference among the regions, which suggests the current total $N(\text{HI})$ is similar toward the three lines. The age of N44 5–6 Myr (Will et al. 1997) makes it difficult to see the initial conditions prior to the collision because the HI gas was significantly dissipated by the high mass stars in 5–6 Myrs. HI gas within 25–30 pc of high-mass stars is dispersed by ionization and stellar winds at an empirical velocity of the ionization front of $\sim 5 \text{ km s}^{-1}$ observed in Galactic high mass clusters (Fukui et al. 2016), and the amount of the HI gas in Line B may be less than the initial value. Thus, HI gas was possibly more concentrated on Line B than Lines A and C before the collision. A scenario that HI gas was further compressed and high-mass stars formed in Line B is consistent with the observations.

We also estimated the total Interstellar medium mass of the star forming region N44 as illustrated by a white dashed circle in Figure 4b. The region is determined so that it includes the H α bubble. The mass of HI is estimated to be $\sim 5 \times 10^5 M_\odot$ by assuming the uniform column density of $\sim 6.0 \times 10^{21} \text{ cm}^{-2}$ (see in Table 3) and the total mass of H $_2$ is $\sim 5 \times 10^5 M_\odot$ by using equation (2). We calculated the approximate total stellar mass of N44 (M^*) as $\sim 1.0 \times 10^5 M_\odot$ assuming the initial mass function (IMF) as follows. IMF varies with mass range of the star (Kroupa 2001) as follows; $\phi(M) dM \propto M^{-2.3} dM$: $M > 0.5 M_\odot$, $\phi(M) dM \propto M^{-1.3} dM$: $M > 0.5 M_\odot > 0.08 M_\odot$, $\phi(M) dM \propto M^{-0.3} dM$: $M > 0.08 M_\odot > 0.01 M_\odot$. When the stellar mass is larger than $0.5 M_\odot$, we adopt $\alpha=2.37$ as the slope of IMF which obtained from BV photometry (Will et al. 1997), and we adopt $\alpha=1.37$ as

the slope of IMF for the stellar mass less than $0.5 M_{\odot}$ (Kroupa 2001). The star formation efficiency (SFE) is about 10% for total interstellar mass ($M(\text{HI}+\text{H}_2)$), where we define SFE as $M^*/(M^*+M(\text{HI}+\text{H}_2))$.

4.2.2. Crossing timescale of collision

We found a spatial displacement between the I- and D-components shown in Figure 9b. We obtained the projected displacement to be 107 pc at a position angle of 180° and the velocity separation is 20 km s^{-1} from Figure 5. More details are given in section 4.2.1. The crossing timescale is estimated to be $\sim 150 \text{ pc} / 28 \text{ km s}^{-1} \sim 5 \text{ Myr}$ by assuming an angle of the cloud relative motion to the line of sight to be $\theta = 45^\circ$. The crossing timescale is consistent with the age of N44 (Will et al. 1997).

We also estimated the crossing timescale of the collision from a ratio of the cloud size and the relative velocity between the two clouds. The apparent spatial extent of the colliding clouds forming high-mass stars is about 200 to 300 pc in Figures 7c. The velocity separation is $\sim 28 \text{ km s}^{-1}$ if we assume the relative motion between the two clouds has an angle of 45° . We calculated a ratio of the cloud size to the relative velocity, giving ~ 7 to 10 Myr as the crossing timescale. The time scale gives a constraint on the upper limit for the age of the high-mass stars formed by colliding HI flows. From these results, we suggest that the crossing timescale is 5–10 Myr, while a younger age is more likely because the deceleration tends to lengthen the timescale than the actual value.

4.3. Inflow of the metal poor gas from the SMC

We found evidence of HI gas inflow from the SMC from the HI and *Planck/IRAS* data (Paper I), and suggest that the HI gas of the SMC is possibly mixed with the HI gas of the LMC by the tidal interaction. Specifically, we derived a gas-dust ratio from a scatter plot between the dust optical depth at 353 GHz (τ_{353}) and the 21 cm HI intensity ($W(\text{HI})$) in the LMC. We used the data with the highest dust temperature which are most probably optically thin HI emission (Fukui et al. 2014b, 2015). The slope of the N44 region in the plot is steeper by $\sim 30\%$ than that of the Bar region which is an older stellar system than the HI Ridge. This difference is interpreted as due to different dust abundance between them.

The results of numerical simulations (Bekki & Chiba 2007b) show that the HI gas of the SMC was mixed with the LMC gas by the close encounter happened 0.2 Gyr ago. If a mixture of the SMC gas and the LMC gas was triggered by the tidal interaction, the N44 region should contain low-metallicity HI gas of the SMC.

If the HI gas of the N44 region consists of HI mass both of the SMC and the LMC at a ratio of 3:7 by assuming that sub-solar metallicity of $1/10 Z_{\odot}$ in the SMC (Rolleston et al. 2003) and of $1/2 Z_{\odot}$ in the LMC (Rolleston et al. 2002), the different slopes in Figure 14 is explained by the mixing. This scenario deserves further pursuit by more elaborated numerical simulations of the hydrodynamical tidal interaction into detail.

4.4. Comparison with the HI Ridge and HI Ridge including R136

We compared physical parameters of N44 and HI Ridge as summarized in Table 3. We see the different physical conditions and the activity of high-mass star formation between N44 and HI Ridge. HI Ridge contain massive stars of R136 in the core of 30 Doradus. The number of high-mass stars of N44 is 10% of HI Ridge (Doran et al. 2013) and the HI intensity of the L-component toward N44 is 25% of the HI Ridge. The spatial extent of the colliding HI flow of N44 is $\sim 25\%$ of the HI Ridge. In addition, we find the I-component toward N44, which has smaller velocity separation than the L-component.

Furthermore, the timescale of the collision is different between N44 and R136. The crossing timescale of N44 is 5–6 Myr, but that of R136 is $\sim 3 \text{ Myr}$ (derived from Paper I). This difference may have been caused by difference in timing of the inflow impact of the tidally driven SMC gas (Bekki & Chiba 2007b).

From these results, we speculate that some physical parameters of the collision, for instance, the amount of the inflow gas from the SMC and the velocity of collision determine the activity of high-mass star formation. However, it is not understood which parameter is important, because we do not have a large number of observational examples and appropriate numerical simulations of the colliding HI flows. We need to study other star forming regions in the LMC as shown in Figure 3 and to carry out statistical analyses more extensively as a future work.

5. CONCLUSION

The main conclusions of the present paper are summarized as follows;

1. We analyzed the high spatial resolution HI data (1 arcmin; corresponding to $\sim 15 \text{ pc}$ at a distance of the LMC) observed by the ATCA & Parkes telescope (Kim et al. 2003), and revealed the spatial and velocity distributions of N44. We confirmed that the two HI components at different velocities, the L- and D-components (Fukui et al. 2017), are colliding at a 500 pc scale with velocity differ-

- ence of ~ 30 to 60 km s^{-1} . The collision is characterized by the spatial complementary distribution and bridge features in velocity space. In addition, we newly defined the I (intermediate)-component between the two velocities as a decelerated gas component due to the collision.
2. We calculated total mass of massive stars (WR and O-type stars) and total mass of the H I gas, and derived star formation efficiency in N44 to be $\sim 10\%$ from a ratio of [the stellar mass]/[the stellar mass plus the H I and CO mass]. A timescale of the collision is estimated by the displacement of the I-component and the velocity difference. We estimated that ~ 5 Myr passed after the collision by assuming that the I-component moved by ~ 100 pc in projection at a velocity of 20 km s^{-1} . This timescale is consistent with an age of the star forming region in N44 (Will et al. 1997). These results suggest it possible that the high-mass stars in N44 were formed by triggering in the colliding H I flows.
 3. We found that the L-component is metal poor as indicated by the low dust optical depth. We estimated the metal content by a comparison of dust optical depth at 353 GHz (τ_{353}) measured by the *Planck/IRAS* and the intensity of H I ($W(\text{H I})$). We derived an indicator of gas-dust ratio ($W(\text{H I})/\tau_{353}$) by the least-squares fitting which is assumed to have a zero intercept. The gas-dust ratio ($W(\text{H I})/\tau_{353}$) of N44 is by 30% larger than that of the Bar region. If the N44 region consists of H I mass from the SMC ($1/10 Z_{\odot}$; Rolleston et al. 2003) and LMC ($1/2 Z_{\odot}$; Rolleston et al. 2002) at a ratio of 3:7, slopes different by 30% in Figure 14 are explained. This result supports the tidal origin of the H I flow and mixing of the SMC gas with the LMC gas as theoretically predicted (Bekki & Chiba 2007b). The H I Ridge is mixed by the H I gas of the SMC and LMC at a ratio of 1:1 (Paper I) and it means the influence of the tidal interaction was weaker in N44 than in the H I Ridge. Since the larger dispersion of the scatter plot between τ_{353} and $W(\text{H I})$ in the Bar region could be results of metal enrichment by star formation history. More detail study of gas-to-dust ratio for the entire LMC will be presented in the upcoming paper (K. Tsuge et al., in preparation).
 4. We compared a collision size scale of the N44 region and that of the H I Ridge, and found that the collision of the N44 region is of a smaller-scale than that of the H I Ridge. Specifically, a spatial extent of the colliding H I flow is about $1/4$ of the H I Ridge

and the intensity of the L-component is weaker by $1/4$ than that of the H I Ridge. It is clearly seen in N44 that the spatial scale of collision, the intensity of blue-shifted H I gas, the number of the formed massive stars, and the H I mass of the inflow from the SMC are smaller than in the H I Ridge.

5. We discussed a scenario that a tidally-driven colliding H I flow triggered the formation of high-mass stars based on the present results. The blue-shifted H I components (the L- and I-velocity components) were formed by a tidal stripping between the LMC and SMC about 0.2 Gyrs ago (Bekki & Chiba 2007a). The perturbed H I gas is colliding with the H I gas in the LMC disk at present. This collision formed ~ 40 O/WR stars in N44 by the same mechanism as in the R136 region (Paper I), but the number of high mass stars of N44 is $\sim 1/10$ as compared with that in R136. The spatial scale of collision and the H I intensity of the blue-shifted components are smaller than H I Ridge, probably because the tidal interaction between the LMC and SMC was weak in the N44 region. More details of the collision are yet to be better clarified for understanding the cause of the difference, and we need to increase the number of the cases where the colliding H I flows trigger high mass star formation in the LMC.

The NANTEN project is based on a mutual agreement between Nagoya University and the Carnegie Institution of Washington (CIW). We greatly appreciate the hospitality of all the staff members of the Las Campanas Observatory of CIW. We are thankful to many Japanese public donors and companies who contributed to the realization of the project. This study was financially supported by JSPS KAKENHI Grant Number 15H05694. This work was also financially supported by Career Development Project for Researchers of Allied Universities. The ATCA, Parkes, and Mopra radio telescope are part of the ATNF which is funded by the Australian Government for operation as a National Facility managed by CSIRO. The UNSW Digital Filter Bank used for the observations with the Mopra Telescope was provided with support from the Australian Research Council. Based on observations obtained with Planck, an ESA science mission with instruments and contributions directly funded by ESA Member States, NASA, and Canada. The Southern H-Alpha Sky Survey Atlas, which is supported by the National Science Foundation. Cerro Tololo Inter-American Observatory (CTIO) is operated by the Association of Universities

for Research in Astronomy Inc. (AURA), under a cooperative agreement with the National Science Foundation (NSF) as part of the National Optical Astronomy Observatories (NOAO). The MCELS is funded through the support of the Dean B. McLaughlin fund at the University of Michigan and through NSF grant 9540747.

APPENDIX

A. DECOMPOSITIONS OF THE L- AND D-COMPONENTS OF HI

To decompose the L- and D-components of HI in the LMC, we used the following method.

1. Verification of spectrum We investigate the velocity structures of HI spectra of the whole LMC by eye. We found that HI spectra are dominated by single-peaked component, with multiple component distributed in some regions.
2. Spectral fitting
 - 1). Searching for a velocity channel that has the strongest intensity of HI spectrum (Figure 16a). We define emission peak with the brightness temperature higher than 20 K as the significant detection.
 - 2). Fitting the HI profile to a Gaussian function. The velocity range used for the fitting is ± 10 channels (~ 16.5 km s $^{-1}$) with respect to the central velocity shown in Figure 16a.
 - 3). The fitting was performed to single Gaussian distribution as follow;

$$f(x) = A_0 \exp\left(-\frac{(v - v_0)^2}{2\sigma^2}\right), \quad (\text{A1})$$

where A_0 , v_0 , and σ are the height, the central velocity, and the velocity dispersion of the Gaussian, respectively set to be free parameters.

- 4). Subtracting Gaussian distribution that obtained by 2) from the original HI spectrum as the residual is shown in Figure 16b.
 - 5). Repeat 1)–4) steps for each spectrum twice.
3. Comparison of the peak velocity

We compared central velocities of the first and second peaks we identified by the above steps for each pixel, and defined the L-component as the components having lower velocity and the D-component having higher velocity. If the above procedure only gives a single velocity component, it is attributed to the D-component. Then, we obtained the central velocity distributions of the L- and D-components.

The velocity distribution of the D-component indicates the rotation of the LMC (Figure 17a). However, we see some local velocity structures differing from the galaxy rotation perturbed by such as SNRs, super bubbles, and supergiant shells. So, we took mean velocity of 500 pc \times 500 pc area by using the median filter for each pixel to remove these influence. Figure 17b shows the smoothed rotation velocity map of the LMC. The disk of the LMC rotate to the west from the east and this result consists with Kim et al. (2003).

4. Subtraction of the galactic rotation velocity

To obtain the velocity relative to the disk rotation velocity (V_{offset}) for each pixel, we subtracted the thus smoothed radial velocity of the D-component (V_D) from the original velocity (V_{LSR}) by shifting the velocity channels.

$$V_{\text{offset}} = V_{\text{LSR}} - V_D \quad (\text{A2})$$

B. ROTATION CURVE OF THE D-COMPONENT

Here we describe the method of deriving the rotation curve of the LMC using the radial velocity map of the D-component as shown in Figure 14b.

1. Magellanocentric radial velocity field

First, we subtract the system velocity of the LMC from the radial velocity of the D-component for each pixel, and define $V_{\text{Magellan},ij}$: $V_{\text{Magellan},ij} = v_{ij} - V_{\text{sys}}$ where $V_{\text{Magellan},ij}$ is Magellanocentric radial velocity of the D-component, v_{ij} is peak velocity of the D-component at the pixel position and V_{sys} is system velocity of the LMC of 252.5 km s^{-1} . The suffix of (i, j) denotes the coordinates along the major and minor axis in Figure 2b.

2. Rotation velocity field

The LMC is almost a face-on galaxy, but it has some inclination angle between the plane of the sky and the plane of the galaxy disk. So, we compensate the velocity gradient due to the inclination. We derive rotation velocity $V_{\text{rot}}(R_{ij})$ at the radius of R_{ij} by using equation (Weaver et al. 1977):

$$V_{\text{rot}}(R_{ij}) = \frac{V_{\text{Magellan}}}{\cos\theta_{ij}\sin I}, \quad (\text{B3})$$

where R_{ij} is the radius from the center on the plane of the galaxy given as $R_{ij} = \sqrt{x^2 + (y/\cos I)^2}$, I is the inclination angle., The minor axis and major axis are drawn with the cyan lines in Figure 2b. θ_{ij} is the angle with respect to the major axis, and position (i, j) .

3. Mask of the region

We masked regions not used for deriving the rotation curve shown as the shaded regions in Figure 2b. Majority of the velocity fields follow a flat disk rotation (Figure 2a). However, there are some regions with velocity deviating from the galaxy rotation. This trend is also suggested by Luks & Rohlf (1992). In order to minimize the local disturbances, we mask the regions with $V_{\text{rot}} \geq 120 \text{ km s}^{-1}$ or $V_{\text{rot}} \leq 0 \text{ km s}^{-1}$. In addition, a $|\theta_{ij}| < 5^\circ$ -sector around the major axis is also masked, because the rotation velocity cannot be determined.

The locally disturbed regions are roughly located at southeast arm (the H I Ridge region) and the northwest arm-end. Their distributions are consistent with the spatial distribution of tidally interacting gas between the LMC and SMC calculated by Bekki & Chiba (2007a) (see also Figure 4 of Bekki & Chiba 2007a). Thus, it is suspected that the local disturbances are due to the tidal interaction.

4. Derivation of rotation curve

We divide the whole region into 16 elliptical annulus whose widths are 0.25 kpc (white ellipses in Figure 2c). We plot the averaged rotation velocity (V_{rot}) for each annulus as a function of the deprojected radial distance $R_{i,j}$ on the plane of the galaxy from the kinematic center of the LMC (red cross in Figure 2d). The error bar in $R_{i,j}$ is the width of the annulus and that in V_{rot} is give as the standard deviation of the rotation velocity in the annulus.

5. Fitting to the flat rotation model

We fitted the plotted data to the flat rotation model expressed as the following tanh function as following equation (Corbelli & Schneider 1997):

$$V_{\text{rot}}(R_{ij}) = V_{\infty} \tanh(R_{ij}/R_0), \quad (\text{B4})$$

where R_0 is the radius where the velocity field change from rigid to flat rotation, and V_{∞} is the circular velocity at $R_{ij} > R_0$.

There are many previous studies of the LMC kinematics as reviewed by Westerlund (1990). Nevertheless the position angle of the major axis and the galaxy inclination are not well determined. The estimated position angles is in the range $\sim 168^\circ$ – 220° and the inclination of 30° – 40° . We decide the best fit values making the reduced

chi-square value given by the rotation curve fittings closest to unity by changing the values of the position angle and inclination, as listed in Table 4.

In addition, we change the value of V_{sys} by 0.5 km s^{-1} step between 245 km s^{-1} and 260 km s^{-1} , and the best fit value is 252.5 km s^{-1} . We also optimized the kinematic center of the LMC (R.A., Dec. = $05^h17.6^m, -69^d2.0^m$). We change the center position by $1'$ step in a region $\pm 4'$ from the center by Kim et al. (1998a), and obtain the best fit value of (R.A., Dec.) = ($05^h16^m24.8^s, -69^d05^m58.9^s$). We summarized the best fit parameters of the kinematic of the LMC in Table 5. The final rotation curve derived by this study is shown in Figure 2c.

6. Median filter

When we subtract the radial velocity of the D-component, we smooth the velocity field by median filter as described in Appendix A, with the size of median filter optimized as follows. We change the size from $50 \times 50 \text{ pc}$ up to $950 \times 950 \text{ pc}$, and adopt $500 \times 500 \text{ pc}$ size as the best choice in this study, based on the value of reduced chi-squared closest to 1 (Table 5).

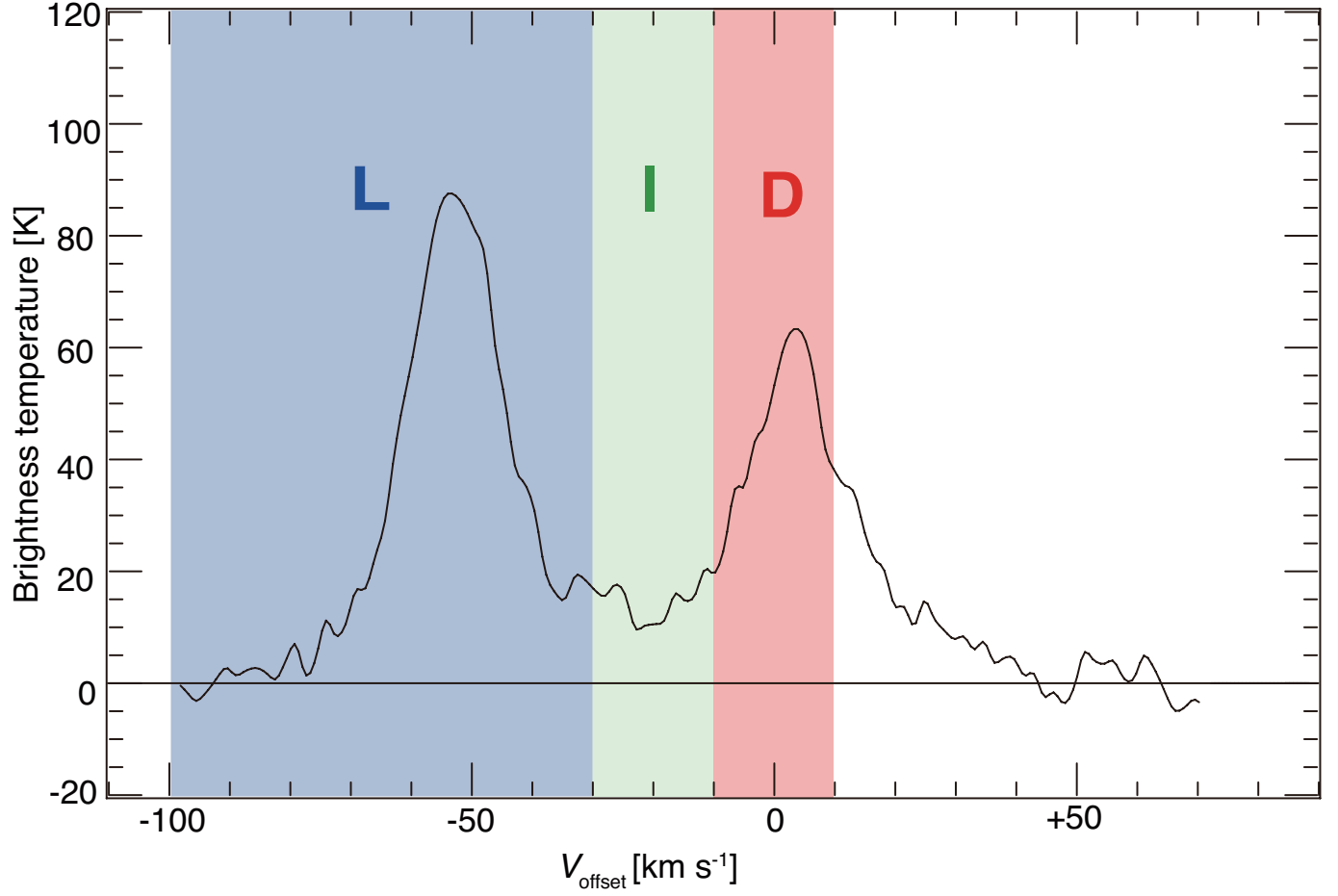


Figure 1. The typical spectra of HI at (R.A., Dec.)=($5^h46^m43.54^s$, $-69^d42^m59.31^s$).

Table 1. Physical properties of HI gas

Region	total mass ($10^5 M_\odot$)	$N(\text{HI})^a$ (10^{21} cm^{-2})	velocity separation (km s^{-1})	I-component (Bridge feature)	# of massive stars ^b
Line A	8.1	5.6	~ 60	yes	2
Line B	9.0	5.9	~ 20	yes	32
Line C	8.1	5.7	$\sim 60 / \sim 20$	yes	5

^aPeak values in each line

^bTotal number of O-type and WR stars.

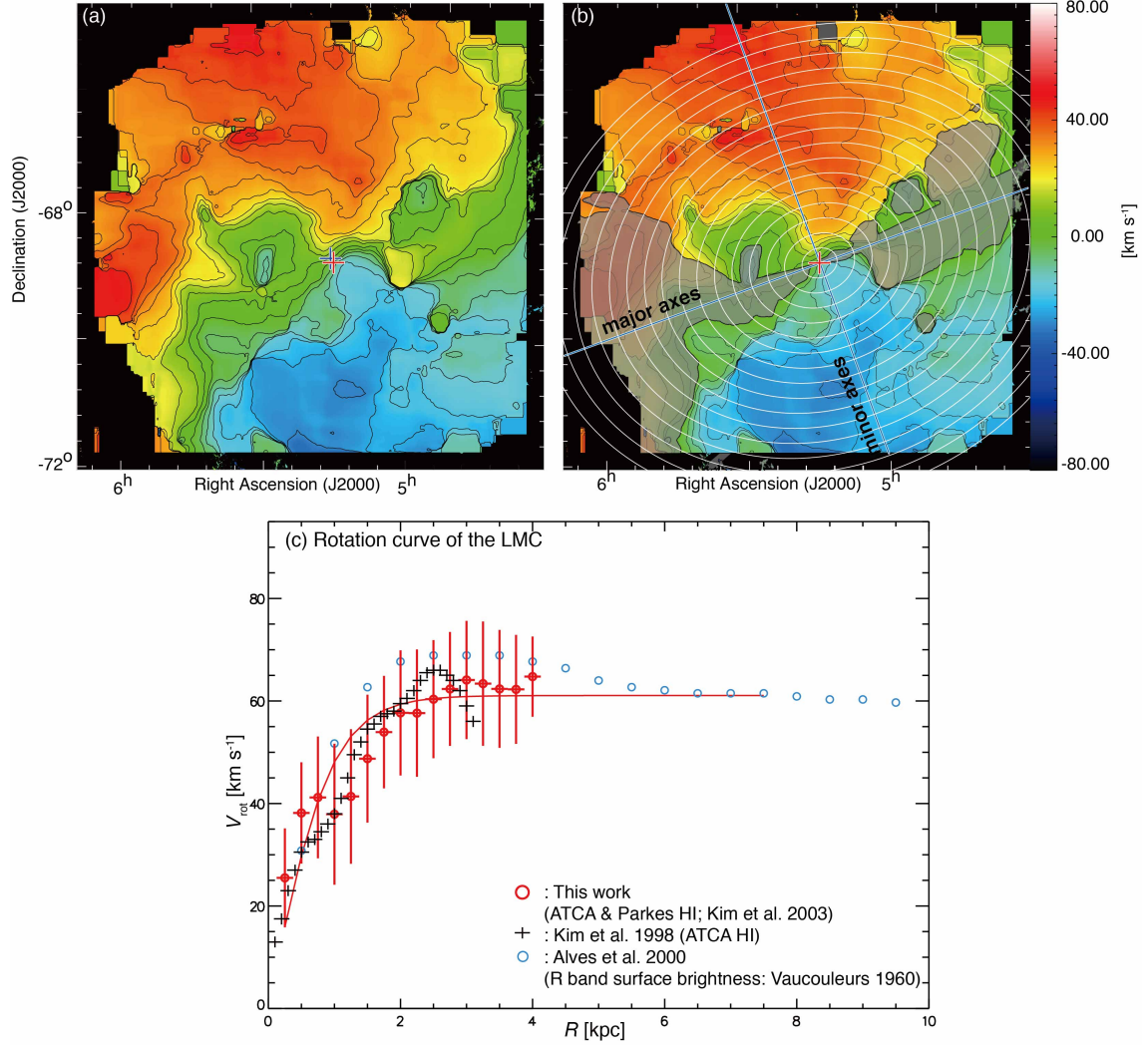


Figure 2. (a) Radial velocity field of the D-component relative to the system velocity of the LMC. This velocity field is smoothed by the median filter with the size of filter of $500 \text{ pc} \times 500 \text{ pc}$. The lowest contour level and intervals are -50 km s^{-1} and 5 km s^{-1} , respectively. The blue and red crosses indicate the positions of kinematic center derived from Kim et al. (1998c) and this study, respectively. The lowest contour level and intervals are 0.25 kpc and 0.25 kpc , respectively. (b) Same image of (a) but superposed with the mask regions (shaded areas). Black contours and red cross are the same as in (a). White ellipses indicate the projected concentric circles around the kinematic center (red cross) on the plane of the galaxy. The cyan lines indicate major and minor axis of the ellipses. (c) Rotation curve of the LMC. The horizontal and vertical axis are radius on the plane of the galaxy and rotation velocity at the radius, respectively. Results of this study are plotted with red open circles. The black crosses indicate the HI data of Kim et al. (1998c). The cyan open circle indicate stellar disk rotation curve derived from the R -band surface brightness data of Alves & Nelson (2000). The mass-to-luminosity ratio is assumed to be constant of 2.2.

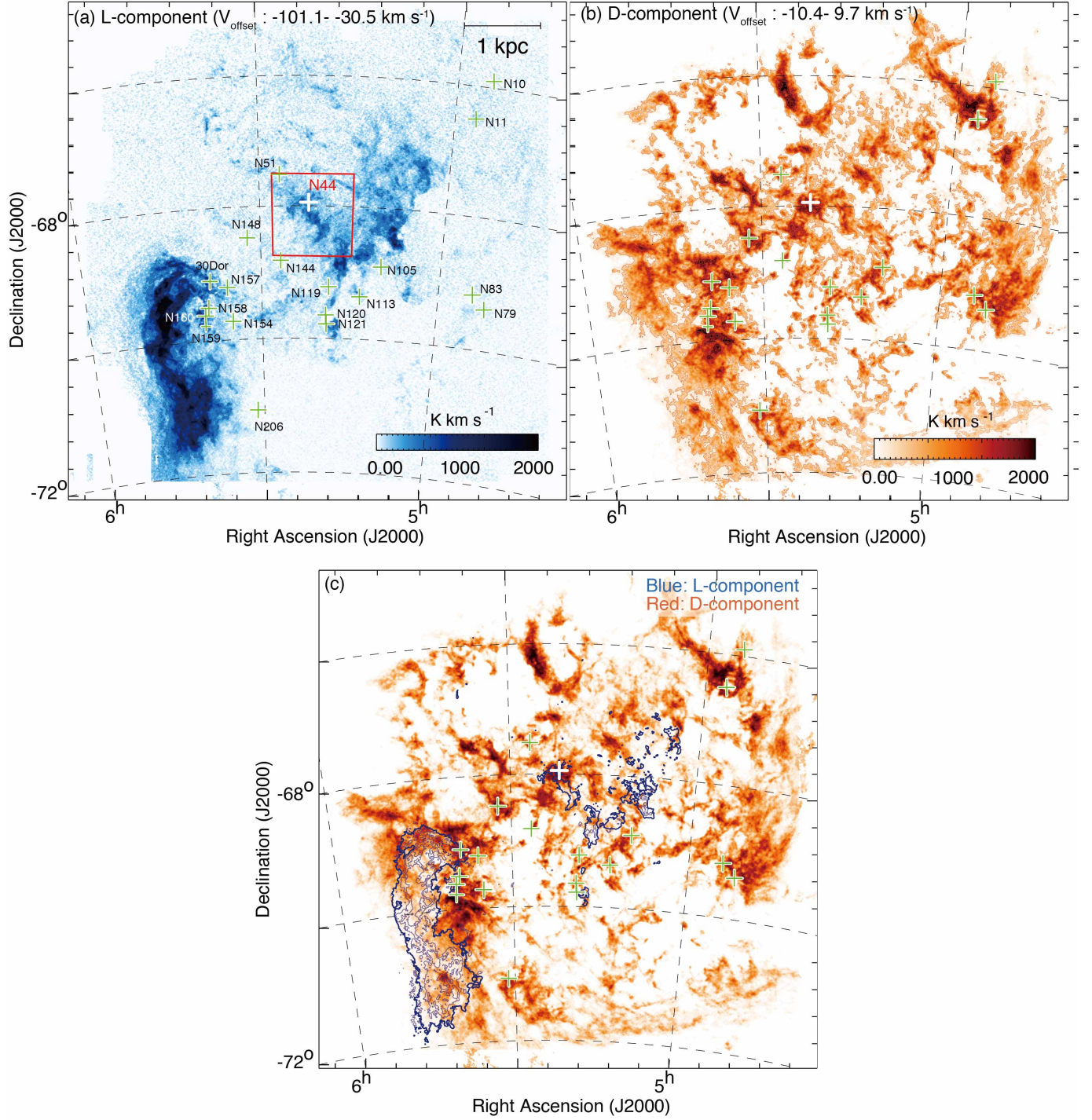


Figure 3. The HI integrated intensity maps of (a) the L-component and (b) the D-component. The integration velocity range is $V_{\text{offset}} = -101.1 - 30.5 \text{ km s}^{-1}$ for the L-component and is $V_{\text{offset}} = -10.4 - 9.7 \text{ km s}^{-1}$ for the D-component. Crosses show the positions of luminous HII regions ($S_{H\alpha} > 1 \times 10^{-4} \text{ erg cm}^{-2} \text{ s}^{-1} \text{ sr}^{-1}$ Ambrocio-Cruz et al. 2016). The red box in (a) denotes the N44 HII region. The contour levels are 350, 800, 1200, and 2400 K km s^{-1} for (a); 400, 800, 1200, 1600, 2000, and 2400 K km s^{-1} for (b). (c) HI intensity map of the L-component by contours superposed on the D-component image. The velocity range and contour levels are the same as in (a) and (b).

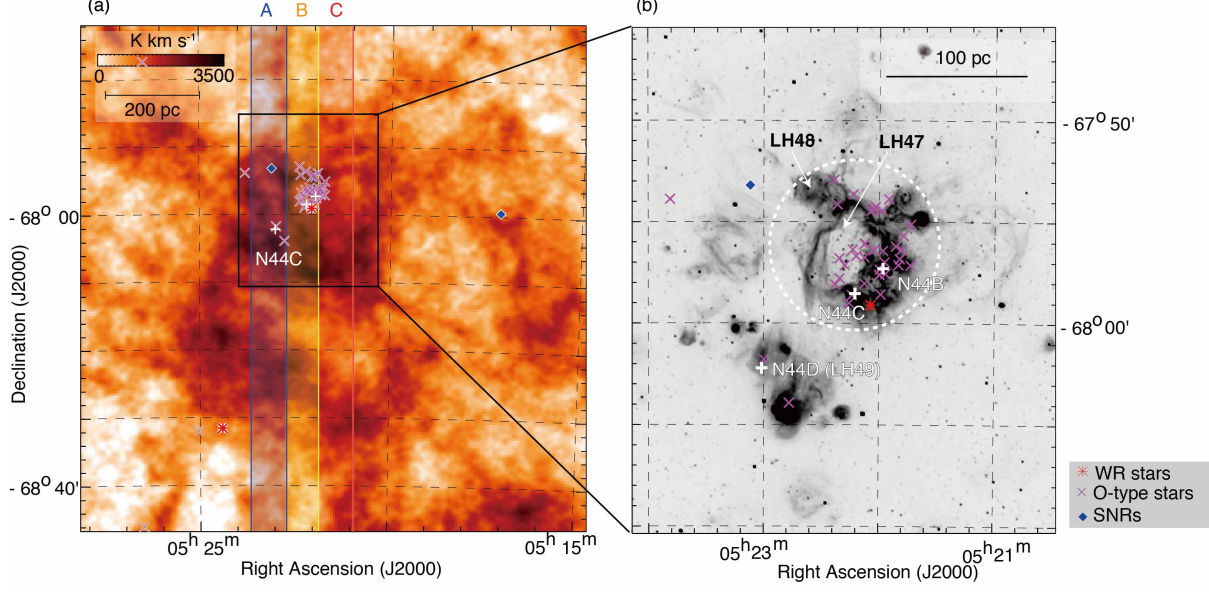


Figure 4. (a) HI total intensity map toward N44. The integration velocity range is $V_{\text{offset}} = -109.8\text{--}89.7 \text{ km s}^{-1}$. Positions-velocity diagrams along the Line A, B, and C passing through the east, center and west of the N44 region are demonstrated in Figure 6, respectively. (b) An enlarged $H\alpha$ image of N44 region. Image is $H\alpha$ (MCEL; Smith & MCELS Team 1999). The red asterisks, pink crosses, and blue diamonds indicate WR stars, O-type stars (Bonanos et al. 2009), and SNRs (Maggi et al. 2016), respectively.

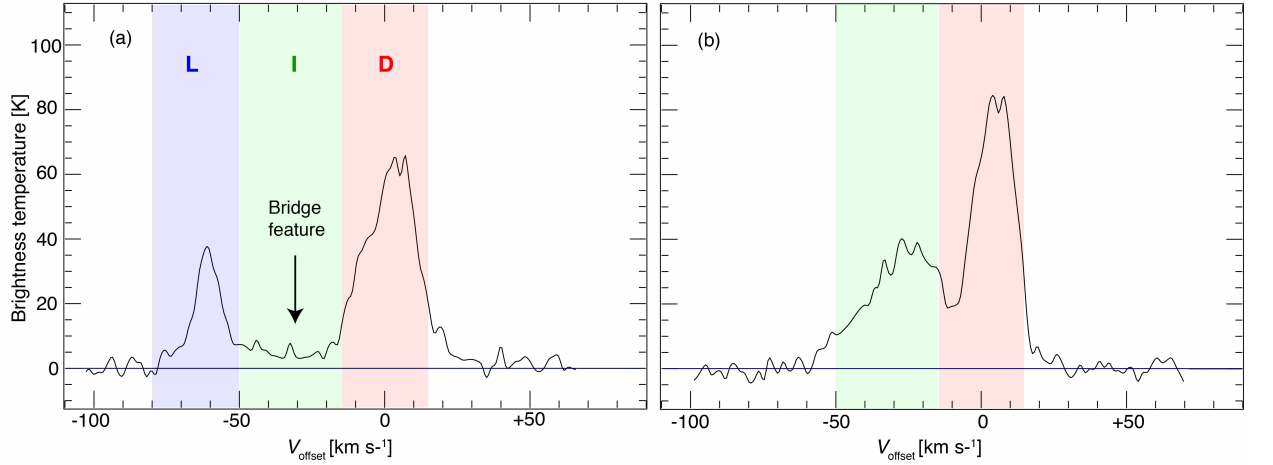


Figure 5. The typical spectra of HI at (a) (R.A., Dec.)= $(5^h 22^m 59.23^s, -67^d 55^m 2.12^s)$ and (b) (R.A., Dec.)= $(5^h 22^m 23.20^s, -68^d 6^m 9.02^s)$. The velocity ranges of shaded area correspond to the integration ranges as shown in Figure 7.

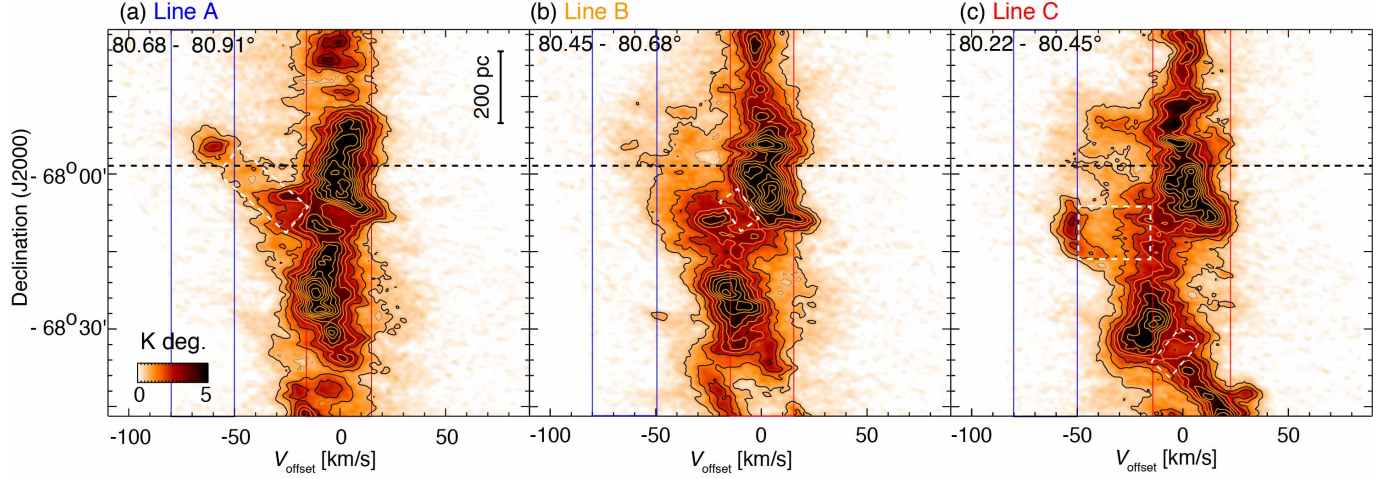


Figure 6. The HI Dec.-velocity diagrams along the lines A, B, and C. The integration is in R.A. over the range from $80^{\circ}68$ to $80^{\circ}91$ for (a); $80^{\circ}45$ to $80^{\circ}68$ for (b); $80^{\circ}22$ to $80^{\circ}45$ for (c). The lowest contour level and intervals are 0.7 K deg. and 0.7 K deg., respectively. Black dashed lines indicate the position of N44C. The white boxes in (a), (b), and (c) indicate the positions of bridge features.

Table 2. Mass of hydrogen gas

	Mass of the L-comp. [M_{\odot}]	Mass of the I-comp. [M_{\odot}]	Mass of the D-comp. [M_{\odot}]	Total mass [M_{\odot}]
HI	1.1×10^5	5.3×10^5	2.0×10^6	3.0×10^6
CO	1.1×10^5	1.0×10^5	2.4×10^6	3.0×10^6

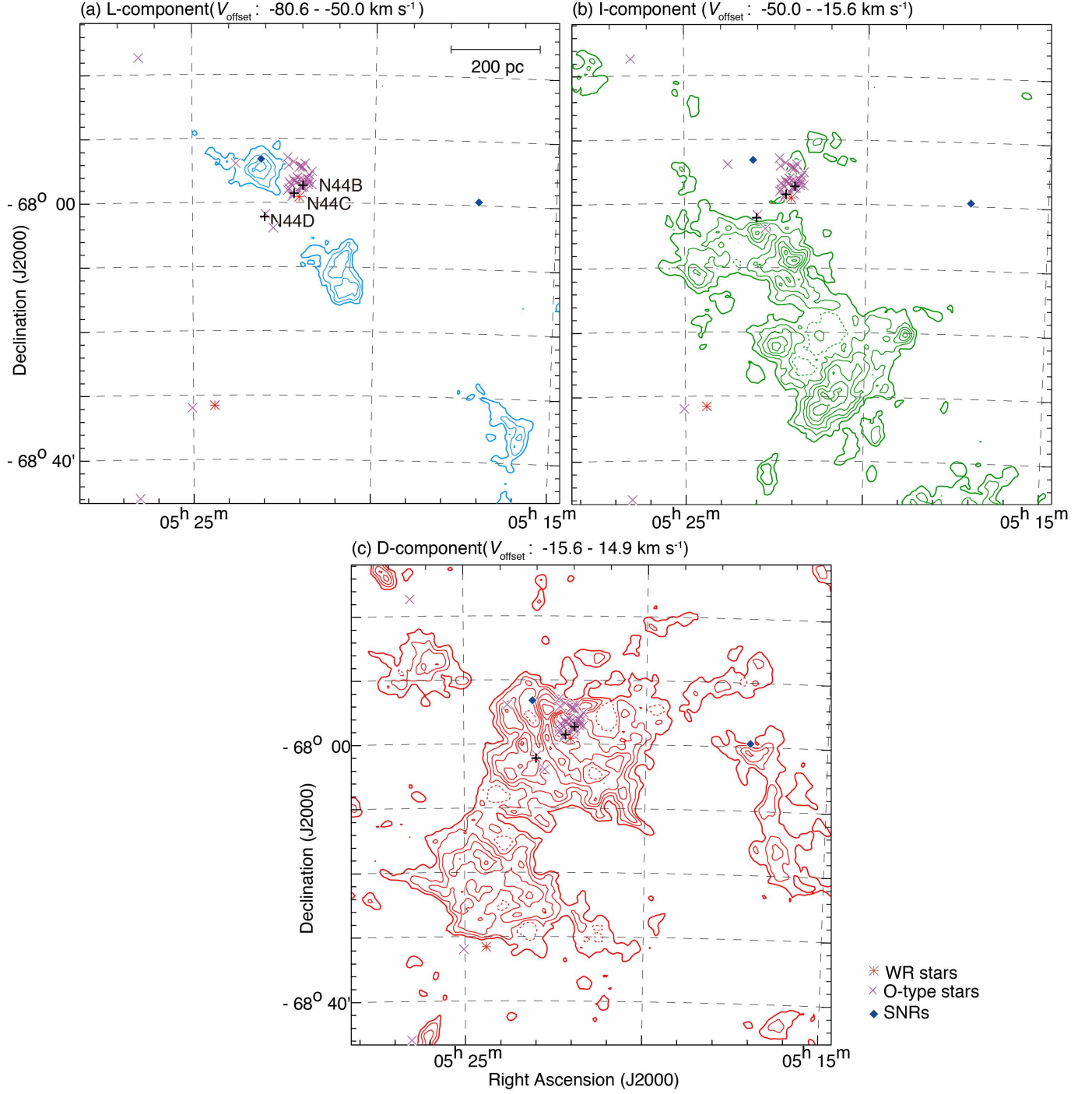


Figure 7. Integrated intensity distributions of HI for the three velocity components shown in Figure 3. The integration range is $V_{\text{offset}} : -80.6 - -50.0 \text{ km s}^{-1}$ for (a); $V_{\text{offset}} : -50.0 - -15.6 \text{ km s}^{-1}$ for (b); $V_{\text{offset}} : -15.6 - 9.7 \text{ km s}^{-1}$ for (c). The lowest contour level and intervals are 200 K km s^{-1} and 100 K km s^{-1} for (a); 500 K km s^{-1} and 150 K km s^{-1} for (b); 1000 K km s^{-1} and 200 K km s^{-1} for (c). The symbols are the same as in Figure 4 (c).

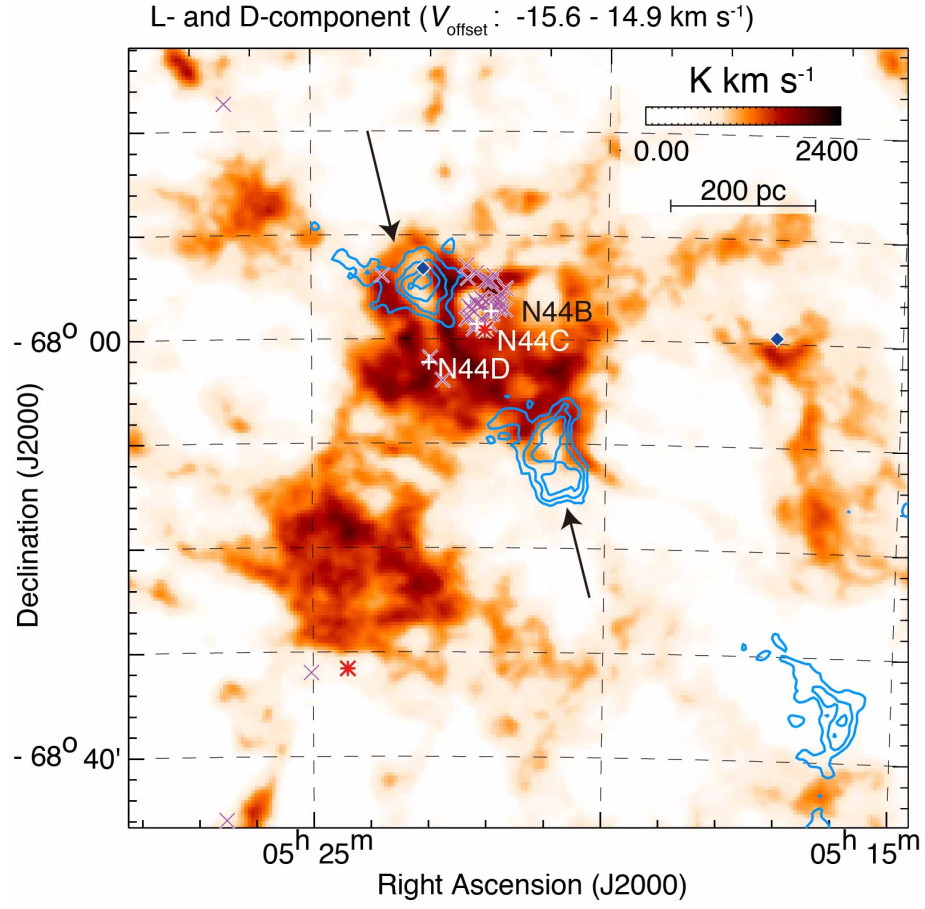


Figure 8. HI intensity maps of the L-component by contours superposed on the D-component by image. The contour levels and symbols are the same as in Figure 4.

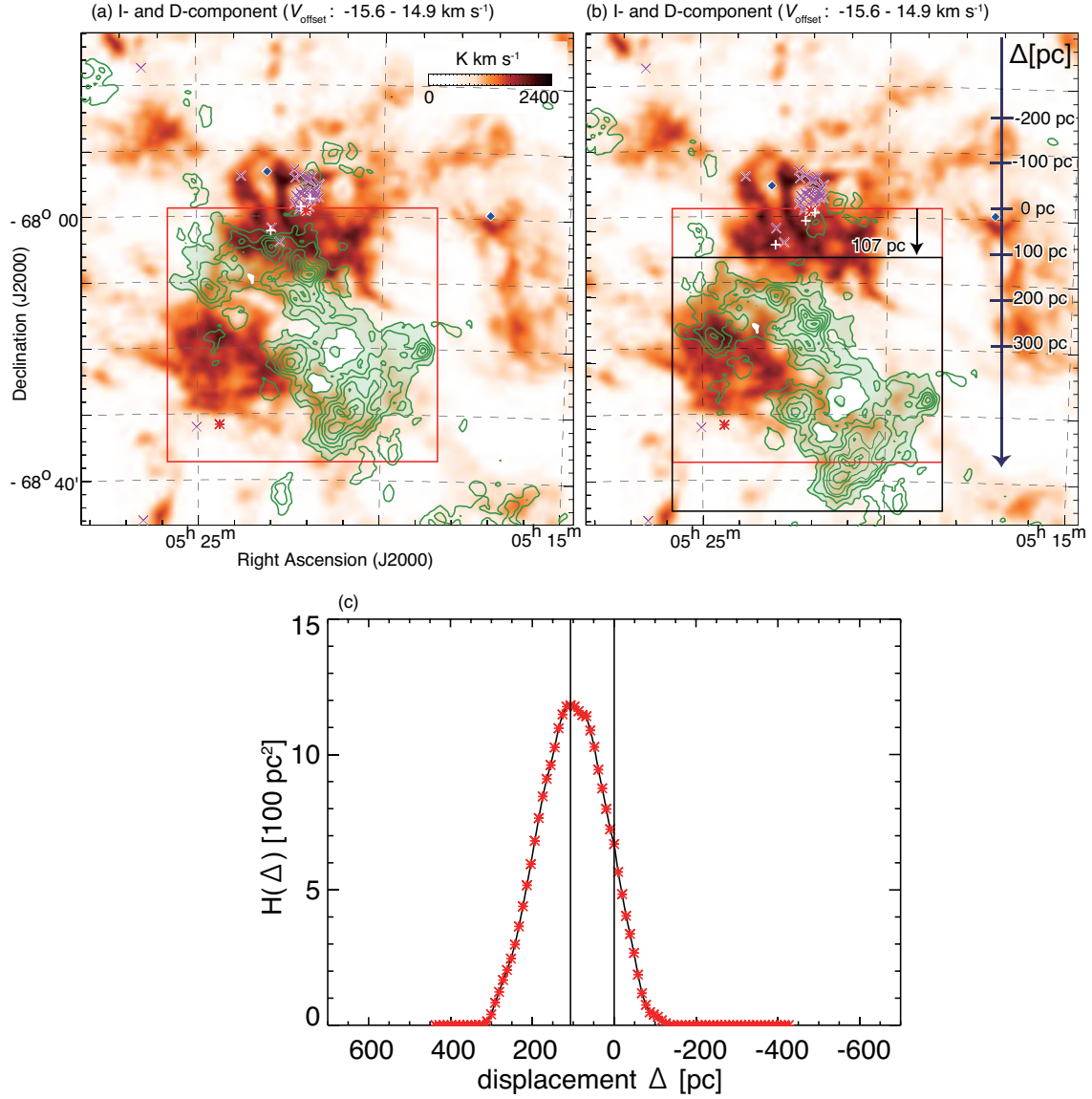


Figure 9. (a) HI intensity maps of the I-component by contours superposed on the D-component by image. (b) Same as (a), but the contours of the I-component are displaced. The projected displacement is 107 pc with a position angle of 180 deg. The red box denotes the initial position of the I-component, and the black box of (b) denotes the displaced position. The green shaded regions of (a) and (b) illustrate the HI intensity of 500 K km s⁻¹ or higher. The contour levels and symbols are the same as in Figure 4. The Δ -axis = 180 deg was taken as the optimum value for the direction of the displacement of the I-component. The origin of Δ -axis denotes the initial position of the I-component. (c) The overlapping integral $H(\Delta)$ in pc² defined in Sec 4.1.3. The strong I-component (> 550 K km s⁻¹) and the depressed D-component (< 1100 K km s⁻¹) were assumed to be a uniform value of 1.0 (arbitrary unit). The horizontal axis is the value displacement Δ [pc] shown in (b).

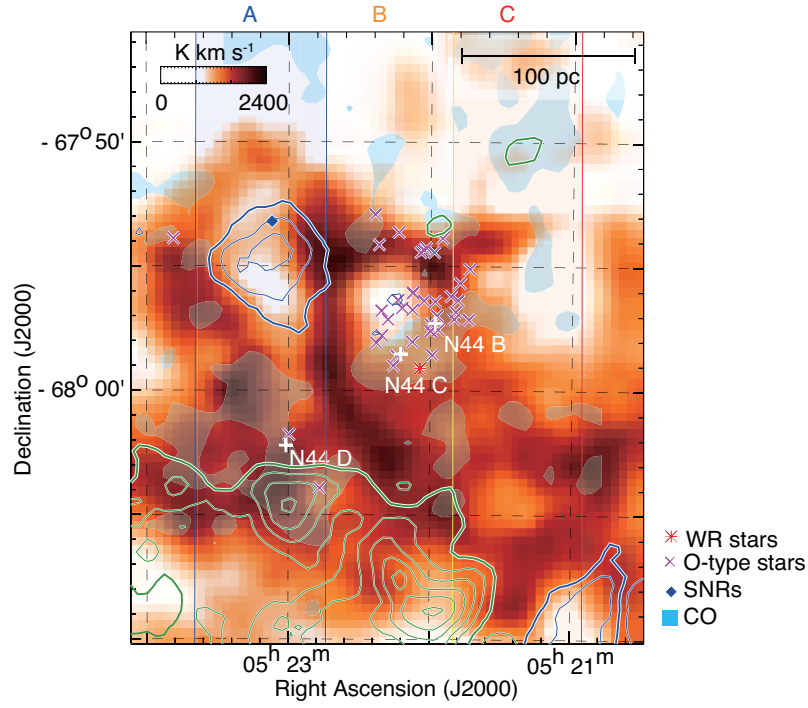


Figure 10. The intensity map of HI consisting of three velocity components around N44. The image indicates the D-component (-15.6 – 14.9 km s^{-1}). The blue and green contours indicate L- and I-components, respectively. The contour levels and symbols are the same as in Figure 7. The light-blue shaded area indicate the integrated intensity map of CO ($> 3\sigma$ (3.5 K km s^{-1}); Wong et al. 2011) with the integration range of V_{offset} : -109.8 – 89.7 km s^{-1}

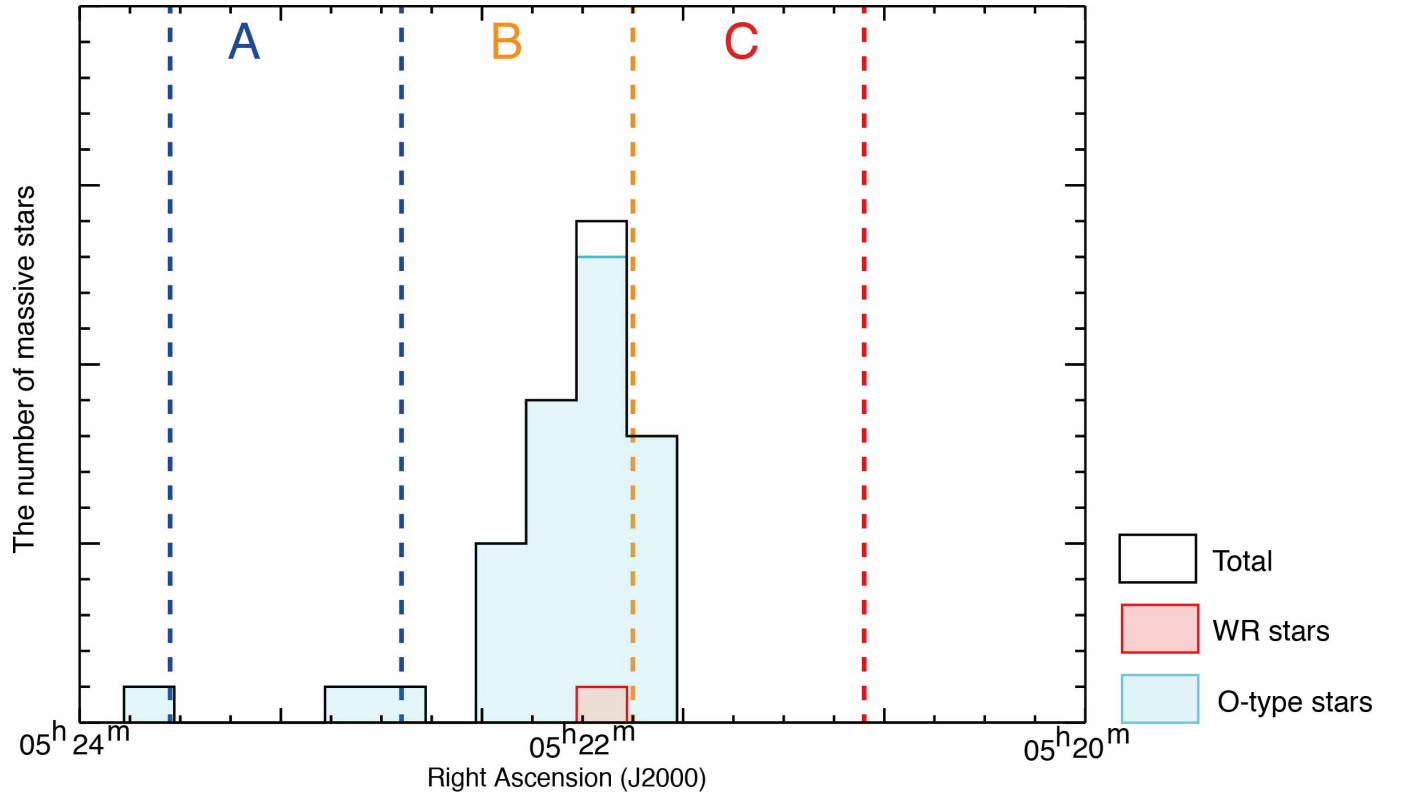


Figure 11. Histograms of the number of massive stars. The horizontal and vertical axis are R.A. and the number of massive stars located within the each R.A. bins, respectively. The histograms of the number of WR stars, O-type stars, and the total number of massive stars are shown by red- and blue-shaded areas, and open area, respectively.

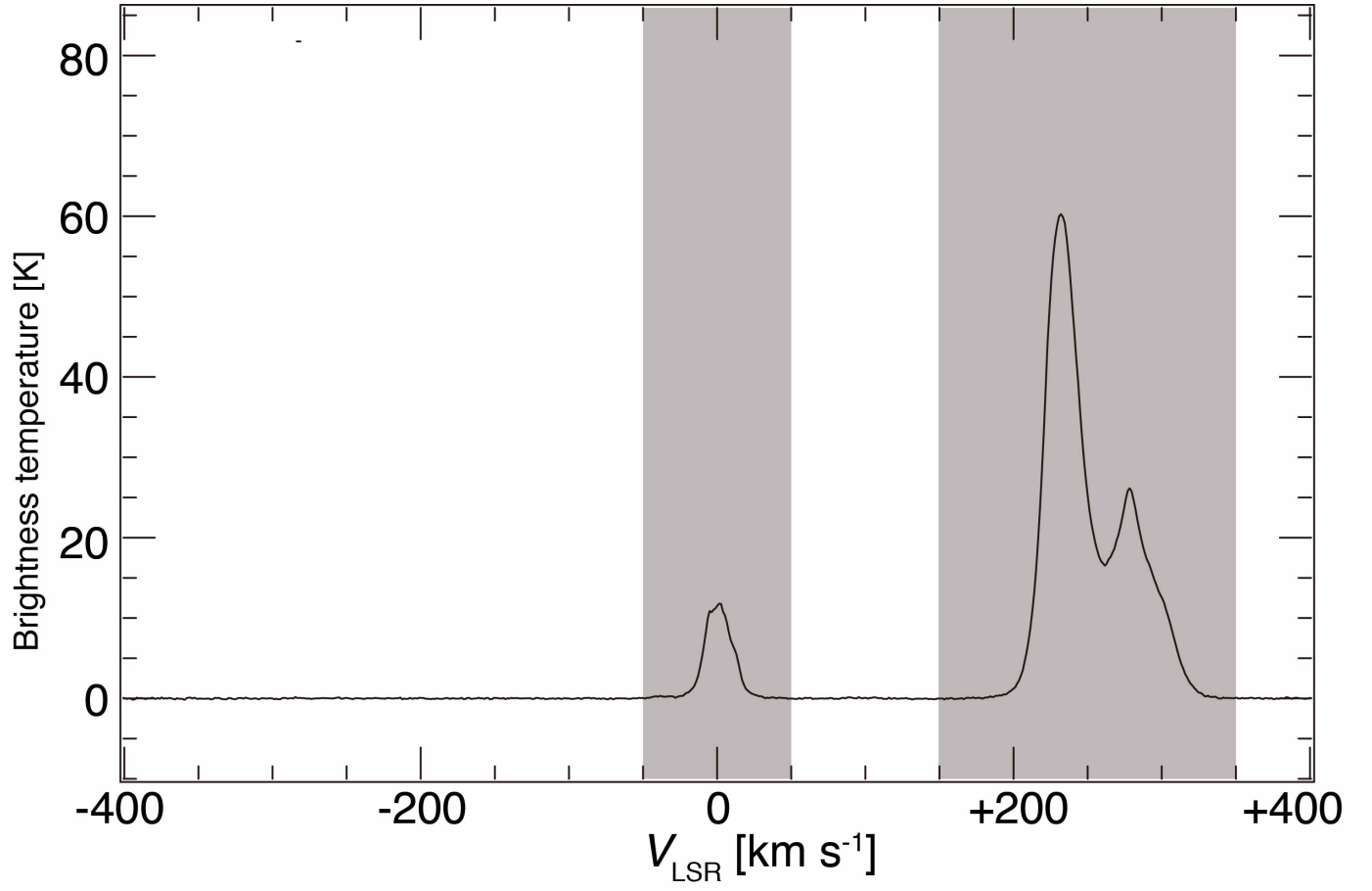


Figure 12. The typical profile of HI spectrum (HI4PI Collaboration et al. 2016) at (R.A., Dec.)=($5^h 45^m 39.09^s$, $-69^d 35^m 41.68^s$).

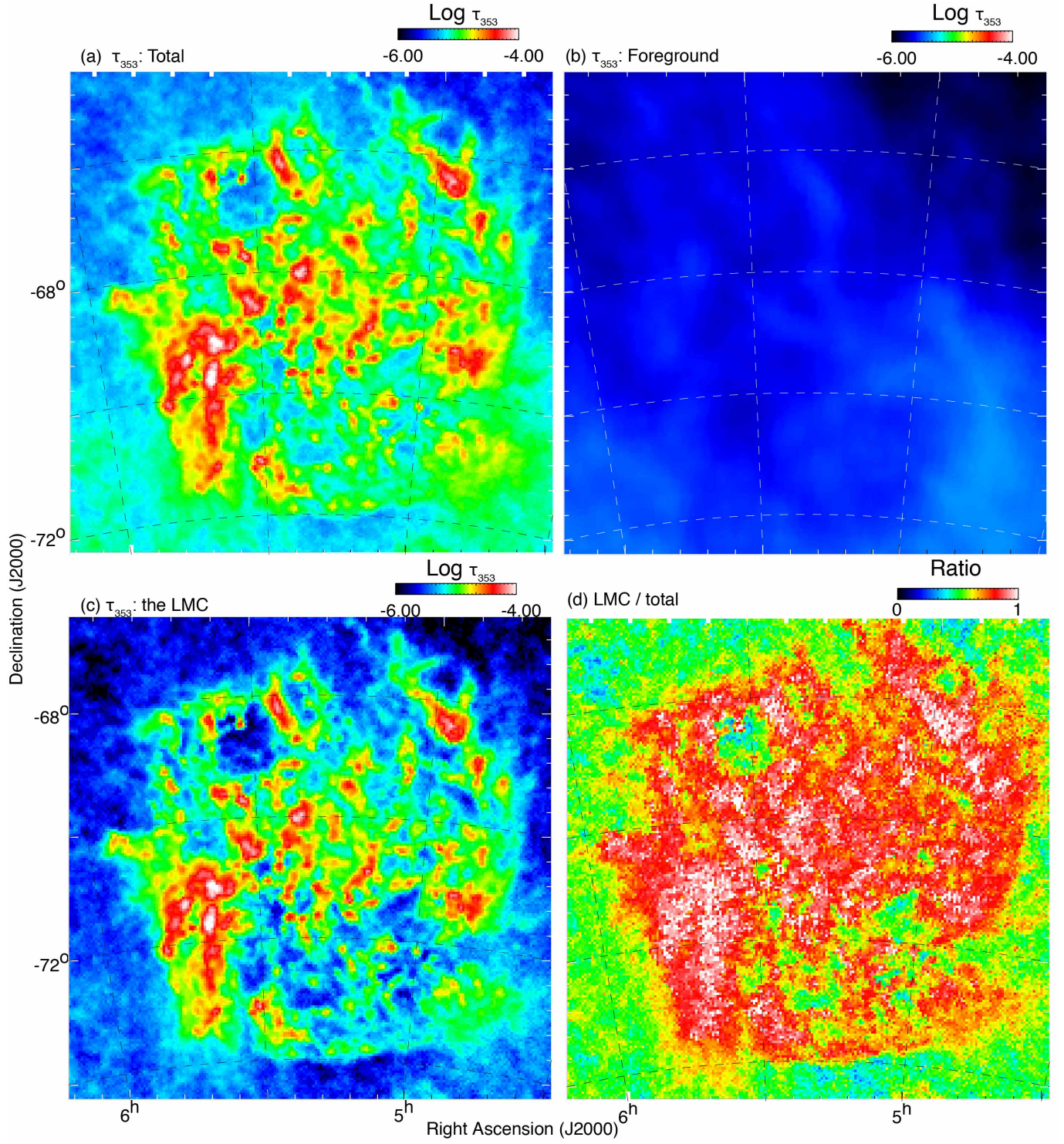


Figure 13. Spatial distribution of τ_{353} toward the LMC. (a), (b), (c), and (d) indicate total quantity of τ_{353} , the Galactic foreground component of τ_{353} , the LMC component of τ_{353} , and the ratio of the LMC component to the total τ_{353} , respectively.

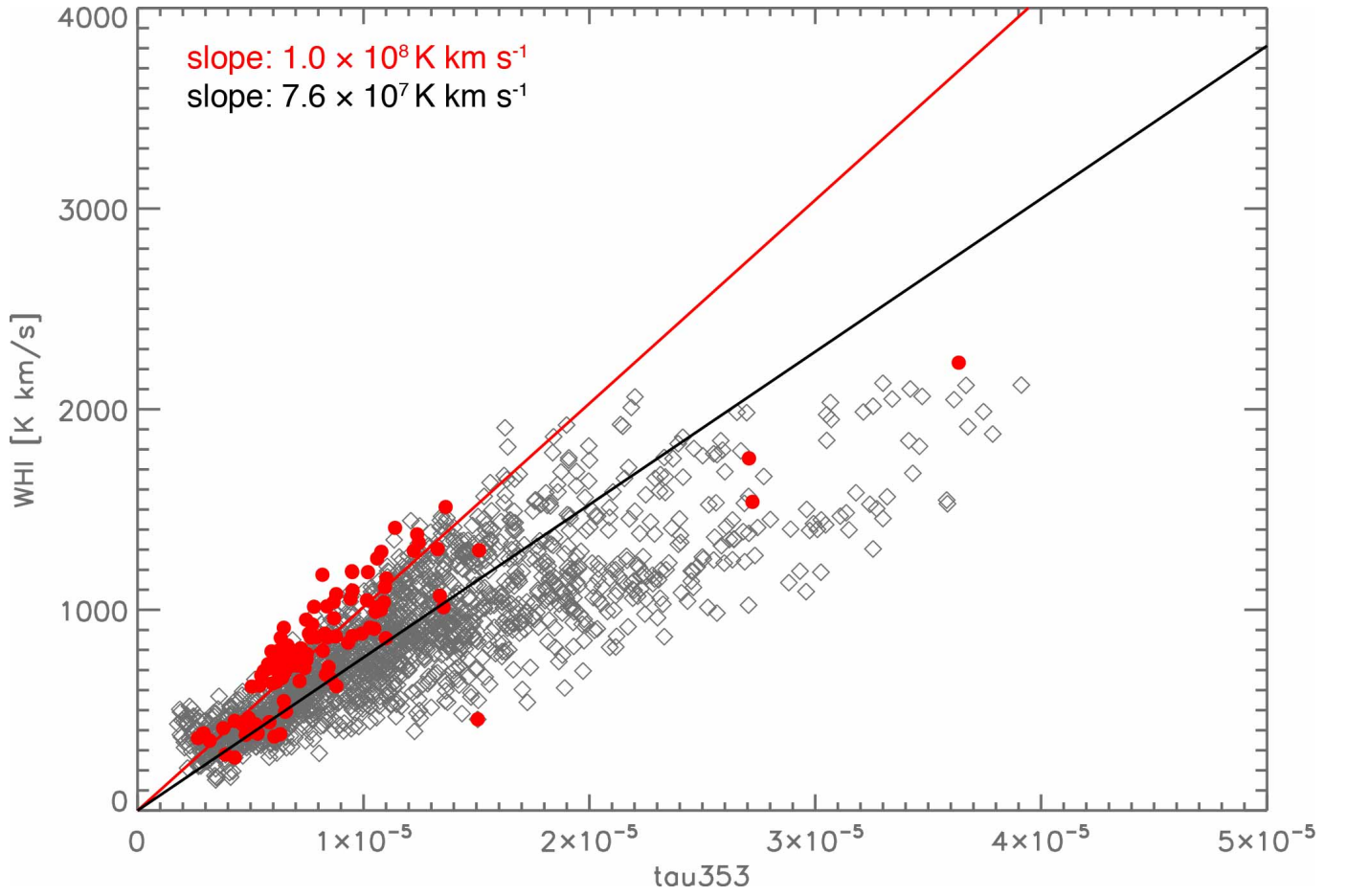


Figure 14. Scatter plot of $W(\text{HI})$ against τ_{353} . The red points are the data with $T_d \geq 24.5 \text{ K}$ in the N44 region (the region of Figure 1(a)), while grey points are the data with $T_d \geq 22.5 \text{ K}$ in the Bar region (Paper I). The red and black linear lines denote the results of the least-squares fits assuming zero intercept toward the Bar region and the N44 region, respectively.

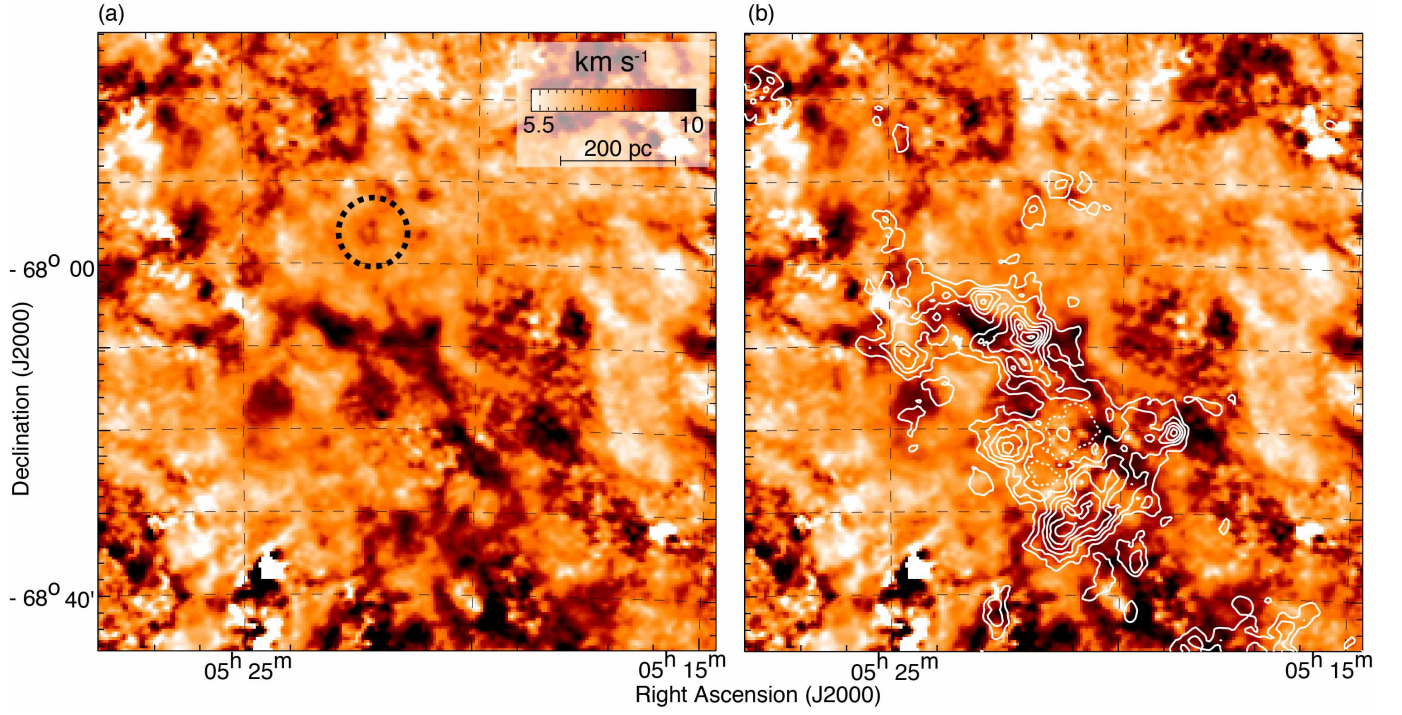


Figure 15. (a) Second moment map of the D-component overlaid with the black dashed circle showing the location of the $\text{H}\alpha$ shell. (b) Same image as (a), but with the contours indicating the I-component. The contour levels are the same as in Figure 7b.

Table 3. Comparison of N44 with H I Ridge including R136

Object	# of O/WR stars	Age [Myr]	Spatial extent of colliding H I gas	fraction of the SMC gas	Column density (max) [10^{22} cm^{-2}]	Total H I mass [M_{\odot}]
(1)	(2)	(3)	(4)	(5)	(6)	(7)
H I Ridge	~ 400	1.5–4.7	$\sim 1 \text{ kpc} \times 2.5 \text{ kpc}$	0.5	1.0	1.0×10^8
N44	~ 40	5–6	$\sim 800 \text{ pc} \times 800 \text{ pc}$	0.3	0.6	2×10^7

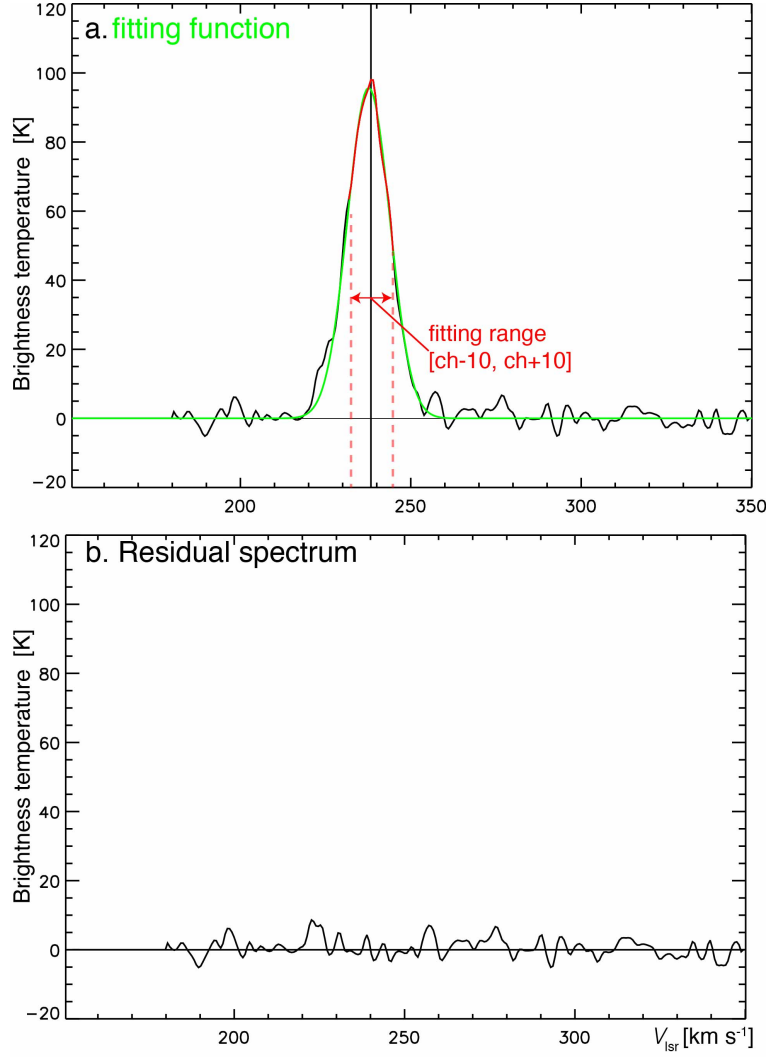


Figure 16. The example of H I spectral fitting. The horizontal and perpendicular axis are velocity and brightness temperature, respectively. (a) Black line indicates the original H I profile. Green and red curved lines indicate the fitting function and H I data used for fitting, respectively. Red dashed lines indicate the fitting range. (b) Residual spectrum of H I spectrum.

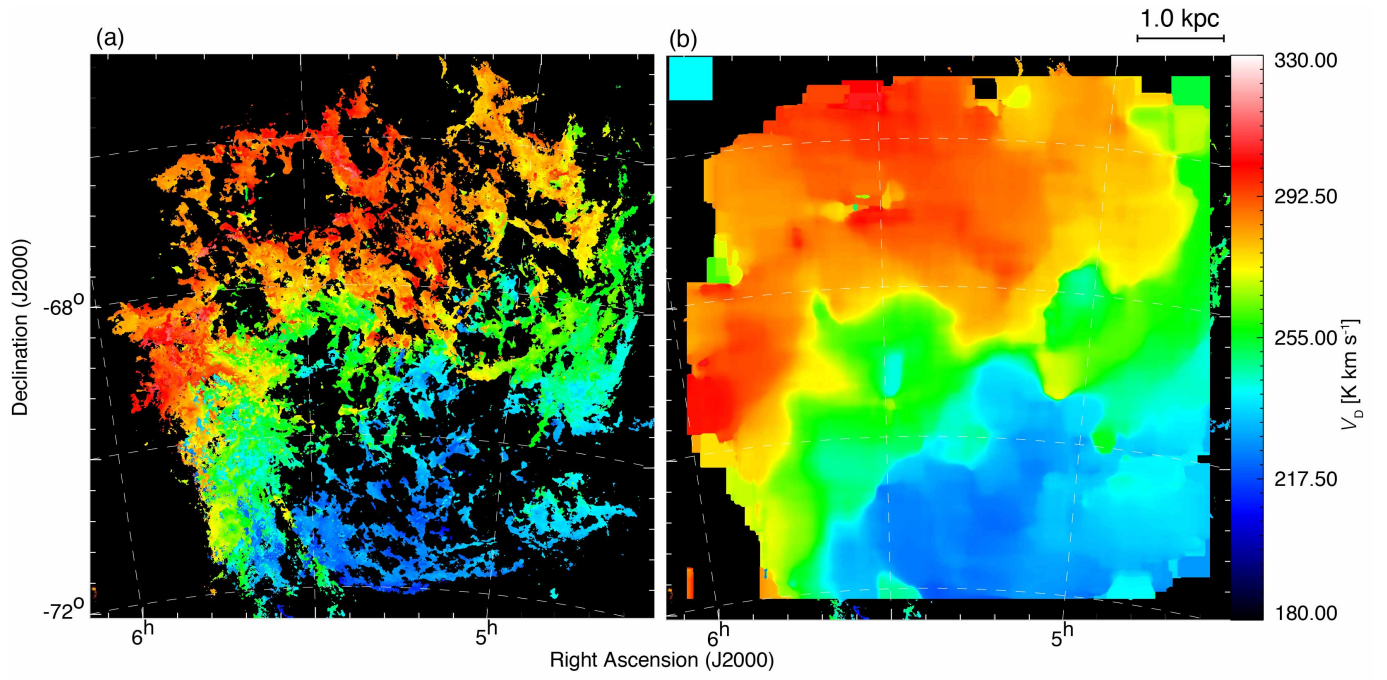


Figure 17. (a) Radial velocity map of the D-component. Black region is masked area with weak H I intensity. (b) Smoothed radial velocity map of the D-component. The size of median filter is also shown in the top left corner.

Table 4. Results of the rotation curve fittings

P.A. [deg.]	Inclination [deg.]	$\chi^2/\text{d.o.f}$	P.A. [deg.]	Inclination [deg.]	$\chi^2/\text{d.o.f}$
(1)	(2)		(3)	(4)	
190	38	1.279	200	38	0.965
	37	1.259		37	0.967
	36	1.246		36	0.978
	35	1.248		35	1.007
	34	1.259		34	1.054
	33	1.275		33	1.146
	32	1.296		32	1.271
195	38	1.208	205	38	0.844
	37	1.189		37	0.865
	36	1.181		36	0.905
	35	1.190		35	0.965
	34	1.218		34	1.054
	33	1.261		33	1.162
	32	1.329		32	1.307

NOTE—Cols. (1)(3): Position Angle of major axis. Cols. (2)(4): Inclination of the rotation axis to the line of sight.

Table 5. The best fit kinematic parameters of the rotation curve

Parameters	values
Kinematic center (R.A., Dec.)	05 ^h 16 ^m 24.82 ^s , −69°05′58.88″
P.A. of major axis [deg.]	200
Inclination [deg.]	35
V_∞ [km s ^{−1}]	61.1
R_0 [kpc]	0.94
V_{sys} [km s ^{−1}]	252.5

Table 6. χ^2 fitting results with different size of the median filter

Filter size	$\chi^2/\text{d.o.f}$
50×50 pc	1.518
200×200 pc	1.267
350×350 pc	0.974
500×500 pc	1.007
650×650 pc	1.039
800×800 pc	0.971
950×950 pc	0.743

REFERENCES

- Alves, D. R., & Nelson, C. A. 2000, *ApJ*, 542, 789
- Ambrocio-Cruz, P., Le Coarer, E., Rosado, M., et al. 2016, *MNRAS*, 457, 2048
- Anathpindika, S. V. 2010, *MNRAS*, 405, 1431
- Baug, T., Dewangan, L. K., Ojha, D. K., & Ninan, J. P. 2016, *ApJ*, 833, 85
- Bekki, K., & Chiba, M. 2007, *PASA*, 24, 21
- Bekki, K., & Chiba, M. 2007, *MNRAS*, 381, L16
- Bonanos, A. Z., Massa, D. L., Sewilo, M., et al. 2009, *AJ*, 138, 1003
- Carlson, L. R., Sewilo, M., Meixner, M., Romita, K. A., & Lawton, B. 2012, *A&A*, 542, A66
- Chen, C.-H. R., Chu, Y.-H., Gruendl, R. A., Gordon, K. D., & Heitsch, F. 2009, *ApJ*, 695, 511
- Corbelli, E., & Schneider, S. E. 1997, *ApJ*, 479, 244
- Crowther, P. A., Caballero-Nieves, S. M., Bostroem, K. A., et al. 2016, *MNRAS*, 458, 624
- Dawson, J. R., McClure-Griffiths, N. M., Wong, T., et al. 2013, *ApJ*, 763, 56
- de Vaucouleurs, G. 1960, *ApJ*, 131, 265
- Dewangan, L. K., Ojha, D. K., Luna, A., et al. 2016, *ApJ*, 819, 66
- Dewangan, L. K., Ojha, D. K., Zinchenko, I., Janardhan, P., & Luna, A. 2017a, *ApJ*, 834, 22
- Dewangan, L. K., Ojha, D. K., & Zinchenko, I. 2017b, *ApJ*, 851, 140
- Dewangan, L. K., Ojha, D. K., Zinchenko, I., & Baug, T. 2018a, *ApJ*, 861, 19
- Dewangan, L. K., Dhanya, J. S., Ojha, D. K., & Zinchenko, I. 2018b, *ApJ*, 866, 20
- Dewangan, L. K. 2017, *ApJ*, 837, 44
- Dickey, J. M., & Lockman, F. J. 1990, *ARA&A*, 28, 215
- Doran, E. I., Crowther, P. A., de Koter, A., et al. 2013, *A&A*, 558, A134
- Dobashi, K., Matsumoto, T., Shimoikura, T., Saito, H., Akisato, K., Ohashi, K., & Nakagomi, K. 2014, *ApJ*, 797, 58
- Enokiya, R., Sano, H., Hayashi, K., et al. 2018, *PASJ*, 70, S49
- Fujimoto, M., & Noguchi, M. 1990, *PASJ*, 42, 505
- Fujita, S., Torii, K., Kuno, N., et al. 2017, *arXiv:1711.01695*
- Fujita, S., Torii, K., Tachihara, K., et al. 2018, *arXiv:1808.00709*
- Fukui, Y., Mizuno, N., Yamaguchi, R., et al. 1999, *PASJ*, 51, 745
- Fukui, Y., Kawamura, A., Minamidani, T., et al. 2008, *ApJS*, 178, 56-70
- Fukui, Y., Kawamura, A., Wong, T., et al. 2009, *ApJ*, 705, 144
- Fukui, Y., & Kawamura, A. 2010, *ARA&A*, 48, 547
- Fukui, Y., Ohama, A., Hanaoka, N., et al. 2014, *ApJ*, 780, 36
- Fukui, Y., Okamoto, R., Kaji, R., et al. 2014, *ApJ*, 796, 59
- Fukui, Y., et al. 2014, *ApJ*, 780, 36
- Fukui, Y., Harada, R., Tokuda, K., et al. 2015, *ApJL*, 807, L4
- Fukui, Y., Torii, K., Onishi, T., et al. 2015, *ApJ*, 798, 6
- Fukui, Y., Torii, K., Ohama, A., et al. 2016, *ApJ*, 820, 26
- Fukui, Y., Tsuge, K., Sano, H., et al. 2017, *PASJ*, 69, L5
- Fukui, Y., et al. 2017, *inprep.*
- Fukui, Y., Torii, K., Hattori, Y., et al. 2018, *ApJ*, 859, 166
- Fukui, Y., Kohno, M., Yokoyama, K., et al. 2018, *PASJ*, 70, S60
- Fukui, Y., Ohama, A., Kohno, M., et al. 2018, *PASJ*, 70, S46
- Fukui, Y., Kohno, M., Yokoyama, K., et al. 2018, *PASJ*, 70, S44
- Furukawa, N., Dawson, J. R., Ohama, A., et al. 2009, *ApJL*, 696, L115
- Gaustad, J. E., McCullough, P. R., Rosing, W., & Van Buren, D. 2001, *PASP*, 113, 132
- Gong, Y., et al. 2017, *ApJL*, 835, L14
- Habe, A., & Ohta, K. 1992, *PASJ*, 44, 203
- Hasegawa, T., Sato, F., Whiteoak, J. B., & Miyawaki, R. 1994, *ApJL*, 429, L77
- Hayashi, K., Sano, H., Enokiya, R., et al. 2018, *PASJ*, 70, S48
- Henize, K. G. 1956, *ApJS*, 2, 315
- HI4PI Collaboration, Ben Bekhti, N., Flöer, L., et al. 2016, *A&A*, 594, A116
- Inoue, T., & Inutsuka, S.-i. 2012, *ApJ*, 759, 35
- Inoue, T., & Fukui, Y. 2013, *ApJ*, 774, L31
- Inoue, T., Hennebelle, P., Fukui, Y., et al. 2018, *PASJ*, 70, S53
- Kawamura, A., Minamidani, T., Mizuno, Y., et al. 2009, *Globular Clusters - Guides to Galaxies*, 121
- Kawamura, A., Mizuno, Y., Minamidani, T., et al. 2010, *VizieR Online Data Catalog*, 218,
- Kim, S., Staveley-Smith, L., Dopita, M. A., et al. 1998, *ApJ*, 503, 674
- Kim, S., Chu, Y.-H., Staveley-Smith, L., & Smith, R. C. 1998, *ApJ*, 503, 729
- Kim, S., Staveley-Smith, L., Sault, R. J., et al. 1998, *IAU Colloq. 166: The Local Bubble and Beyond*, 506, 521
- Kim, S., Staveley-Smith, L., Dopita, M. A., et al. 2003, *ApJS*, 148, 473
- Kobayashi, M. I. N., Kobayashi, H., Inutsuka, S.-i., & Fukui, Y. 2018, *PASJ*, 70, S59

- Kohno, M., Torii, K., Tachihara, K., et al. 2018, PASJ, 70, S50
- Kohno, M., Tachihara, K., Fujita, S., et al. 2018, arXiv:1809.00118
- Kroupa, P. 2001, MNRAS, 322, 231
- Kruijssen, J. M. D. 2012, MNRAS, 426, 3008
- Li, C., Wang, H., Zhang, M., et al. 2018, ApJS, 238, 10
- Loren, R. B. 1976, ApJ, 209, 466
- Luks, T., & Rohlfs, K. 1992, A&A, 263, 41
- Maggi, P., Haberl, F., Kavanagh, P. J., et al. 2016, A&A, 585, A162
- Meaburn, J., & Laspias, V. N. 1991, A&A, 245, 635
- Miyawaki, R., Hayashi, M., & Hasegawa, T. 1986, ApJ, 305, 353
- Miyawaki, R., Hayashi, M., & Hasegawa, T. 2009, PASJ, 61, 39
- Mizuno, N., Yamaguchi, R., Mizuno, A., et al. 2001, PASJ, 53, 971
- Nakamura, F., et al. 2012, ApJ, 746, 25
- Nakamura, F., et al. 2014, ApJL, 791, L23
- Nishimura, A., et al. 2017a, arXiv:1706.06002
- Nishimura, A., Minamidani, T., Umemoto, T., et al. 2018, PASJ, 70, S42
- Nishimura, A., et al. 2017c, in prep.
- Oey, M. S., & Massey, P. 1995, ApJ, 452, 210
- Okamoto, R., Yamamoto, H., Tachihara, K., et al. 2017, ApJ, 838, 132
- Ohama, A., Dawson, J. R., Furukawa, N., et al. 2010, ApJ, 709, 975
- Ohama, A., et al. 2017a, arXiv:1706.05652
- Ohama, A., Kohno, M., Fujita, S., et al. 2018, PASJ, 70, S47
- Ohama, A., Kohno, M., Hasegawa, K., et al. 2018, PASJ, 70, S45
- Okumura, S.-I., Miyawaki, R., Sorai, K., Yamashita, T., & Hasegawa, T. 2001, PASJ, 53, 793
- Planck Collaboration, Abergel, A., Ade, P. A. R., et al. 2014, A&A, 571, A11
- Putman, M. E., Gibson, B. K., Staveley-Smith, L., et al. 1998, Nature, 394, 752
- Rolleston, W. R. J., Trundle, C., & Dufton, P. L. 2002, A&A, 396, 53
- Rolleston, W. R. J., Venn, K., Tolstoy, E., & Dufton, P. L. 2003, A&A, 400, 21
- Saigo, K., Onishi, T., Nayak, O., et al. 2017, ApJ, 835, 108
- Sano, H., et al. 2017b, arXiv:1708.08149
- Sano, H., Enokiya, R., Hayashi, K., et al. 2018, PASJ, 70, S43
- Sato, F., Hasegawa, T., Whiteoak, J. B., & Miyawaki, R. 2000, ApJ, 535, 857
- Schneider, F. R. N., Sana, H., Evans, C. J., et al. 2018, Science, 359, 69
- Shimoikura, T., & Dobashi, K. 2011, ApJ, 731, 23
- Shimoikura, T., et al. 2013, ApJ, 768, 72
- Smith, R. C., & MCELS Team 1999, New Views of the Magellanic Clouds, 190, 28
- Staveley-Smith, L. 1997, PASA, 14, 111
- Tachihara, K., Gratier, P., Sano, H., et al. 2018, PASJ, 70, S52
- Takahira, K., Tasker, E. J., & Habe, A. 2014, ApJ, 792, 63
- Tan, J. C., Beltrán, M. T., Caselli, P., et al. 2014, Protostars and Planets VI, 149
- Torii, K., Enokiya, R., Sano, H., et al. 2011, ApJ, 738, 46
- Torii, K., Hasegawa, K., Hattori, Y., et al. 2015, ApJ, 806, 7
- Torii, K., Hattori, Y., Hasegawa, K., et al. 2017, ApJ, 835, 142
- Torii, K., et al. 2017b, ApJ, 840, 111
- Torii, K., et al. 2017c, arXiv:1706.07164
- Torii, K., Fujita, S., Matsuo, M., et al. 2018, PASJ, 70, S51
- Tsuboi, M., Miyazaki, A., & Uehara, K. 2015, PASJ, 67, 109
- Tsutsumi, D., et al. 2017, arXiv:1706.05664
- Weaver, R., McCray, R., Castor, J., Shapiro, P., & Moore, R. 1977, ApJ, 218, 377
- Westerlund, B. E. 1990, A&A Rv, 2, 29
- Will, J.-M., Bomans, D. J., & Dieball, A. 1997, A&AS, 123,
- Wong, T., Hughes, A., Ott, J., et al. 2011, ApJS, 197, 16
- Yozin, C., & Bekki, K. 2014, MNRAS, 443, 522
- Zinnecker, H., & Yorke, H. W. 2007, ARA&A, 45, 481